POLITECNICO DI TORINO

Master's Degree in Physics of Complex Systems

Master's Degree Thesis

Non-equilibrium crystallisation across a dynamical phase transition

Supervisors

Prof. Ludovic BERTHIER

Prof. Luca DALL'ASTA

Candidate

Leonardo GALLIANO

October 2022

Abstract

Dynamical phase transitions are non-equilibrium phenomena characterised by the non-analytical behaviour of some physical quantity. These processes share many features with equilibrium transitions, first and foremost the concept of universality. A lot of interest has been attracted in recent years by a special class of dynamical transitions, called absorbing phase transitions. Many processes ranging from fluids percolating through a medium to the spread of epidemics can be studied in the framework of absorbing phase transitions. These systems exhibit a dynamical transition from an active phase, where the order parameter fluctuates around a non-zero value, to an inactive phase, where the system is trapped into an absorbing state with no activity at all. In this thesis we discuss the properties of a numerical model of two-dimensional monodisperse interacting particles that exhibits an absorbing phase transition at high densities. The main feature of our model is that particles self-organise on the sites of a hexagonal lattice in a specific region of parameter space. The aim of this dissertation is to investigate the interplay between crystallisation and the absorbing phase transition. We study the universality class of this model by measuring several quantities and estimating critical exponents. We then focus on the ordering transition and we discuss its similarities with equilibrium crystallisation. Finally, we show that the non-equilibrium protocol defining our model can generate two dimensional crystals with long-range translational order, which cannot exist at equilibrium.

Keywords: Random organisation, self-organisation, absorbing phase transitions, two-dimensional crystallisation

Table of Contents

Chapter 1

Non-equilibrium processes

When a system is in thermodynamic equilibrium nothing changes from a macroscopic point of view. Taking advantage of this property, equilibrium Statistical Mechanics, proved to be extremely successful at describing physical phenomena. Introducing a description of complex systems based on probability distributions over ensembles has allowed to give a precise meaning to the well-known laws of thermodynamics and, ultimately, to explain the mechanisms that govern phase transitions [1, 2].

However, most physical systems, ranging from electrons in a wire to human cells are out of equilibrium. These systems are notoriously more difficult to treat, since an important part of the methods and techniques used to study equilibrium phenomena breaks down. Nonetheless, many concepts of Statistical Mechanics such as extensivity, symmetry breaking, scaling and universality arise from the idea of 'macroscopicity' and hold even far from equilibrium [3].

In this chapter we introduce two methods that have proven to be very successful in modeling out of equilibrium systems, by following lecture notes of David Tong [2] and Jorge Kurchan [3]. The first method deals with the evolution of probability distributions over configuration space, while the second one is based on stochastic

differential equations. In the last part of the chapter, we show how these two seemingly different methods are related and we use the underlining connection to give an insightful interpretation to the notion of detailed balance.

1.1 Markov chains and detailed balance

A classical way of describing non-equilibrium phenomena is a representation in terms of a stochastic process over the space $\mathcal{X}$ of microscopic configurations. The most famous example is the Markov chain, a discrete-time stochastic process such that the probability to 'jump' from the current state X_t to the subsequent one X_{t+1} depends only on X_t. This property makes Markov processes very suitable to describe physical systems with a finite correlation time. A Markov chain is defined by its transition matrix

$$\mathcal{P}_{X\to X'} = \mathbb{P}(X_{t+1} = X' | X_t = X), \quad \forall X, X' \in \mathcal{X}, \tag{1.1}$$

with

$$\sum_{X'\in\mathcal{X}} \mathcal{P}_{X\to X'} = 1. \tag{1.2}$$

Once $\mathcal{P}$ is specified, the probability distribution over the system's configurations

$$P(X,t) = \mathbb{P}(X_t = X) \tag{1.3}$$

is determined by

$$P(X',t) = \sum_{X\in\mathcal{X}} \mathcal{P}_{X\to X'} P(X,t-1). \tag{1.4}$$

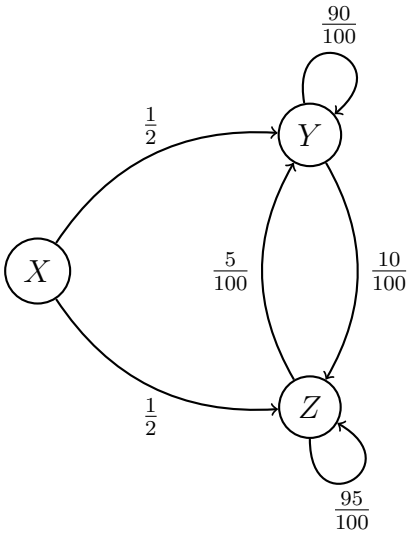

Figure 1.1: Example of Markov chain.

1.1.1 Stationary distribution

A Markov chain is ergodic if it is possible to eventually get from every state to every other state with positive probability [4]. If the Markov chain is ergodic, then there exists a unique stationary probability distribution P_s such that

$$\lim_{t\to+\infty} P(X,t) = P_s, \tag{1.5}$$

for every initial distribution $P(X_0,\, 0)$. Since P_s is stationary,

$$P_s(X') = \sum_{X\in\mathcal{X}} \mathcal{P}_{X\to X'}\, P_s(X). \tag{1.6}$$

This property can be rewritten as

$$\sum_{X\in\mathcal{X}} \mathcal{P}_{X'\to X}\, P_s(X') = \sum_{X\in\mathcal{X}} \mathcal{P}_{X\to X'}\, P_s(X), \tag{1.7}$$

which is known as the balance condition. It means that, in the steady state, probability currents should balance so that outgoing and incoming flows are equal for each configuration. Notice that (1.7) does not forbid currents between different

configurations, hence P_s can describe steady states that are out of equilibrium. In this thesis we will be mainly interested in studying some of these non-equilibrium steady states.

1.1.2 Equilibrium steady state

Suppose now that a Markov chain satisfies

$$\mathcal{P}_{X'\to X}\, P_s(X') = \mathcal{P}_{X\to X'}\, P_s(X), \quad \forall X, X' \in \mathcal{X}. \tag{1.8}$$

This is the detailed balance condition, which requires currents to vanish between each pair of connected configurations and can be interpreted as a microscopic definition of equilibrium. Of course, if a system satisfies (1.8), then (1.7) trivially holds.

Remark. Detailed balance was first introduced as a method for efficient sampling of equilibrium configurations in computer simulations. Since the equilibrium probability $P_s = P_{\text{eq}}$ is known to be the Bolzmann distribution, (1.8) can be seen as a rule for the transition probabilities

$$\frac{\mathcal{P}_{X'\to X}}{\mathcal{P}_{X\to X'}} = \frac{P_{\text{eq}}(X)}{P_{\text{eq}}(X')}. \tag{1.9}$$

A famous choice for $\mathcal{P}_{X\to X'}$ is given by the Metropolis-Hasting algorithm, which uses

$$\mathcal{P}_{X\to X'} = \min\left\{1,\, \frac{P_{\text{eq}}(X')}{P_{\text{eq}}(X)}\right\}. \tag{1.10}$$

1.2 The Langevin equation

In 1827 Robert Brown observed that a mesoscopic particle suspended in water experiences a random jittering motion [5]. We know now this phenomenon being caused by the constant collisions of the particle with the surrounding liquid molecules. To

model this process, consider a particle of mass m in a fluid of viscosity ζ. If the external forces acting on the particle arise from a known potential V, its dynamics can be described by

$$m\ddot{\boldsymbol{x}}(t) = -\zeta \boldsymbol{x}(t) - \boldsymbol{\nabla} V + \boldsymbol{\eta}(t), \tag{1.11}$$

where $\boldsymbol{\eta}$ is a white Gaussian noise, i.e. a random process with probability distribution

$$\mathcal{P}[\boldsymbol{\eta}(t)] = \frac{1}{\mathcal{N}} \, \mathrm{e}^{-\frac{1}{4B}\int_{\mathbb{R}} \|\boldsymbol{\eta}\|^2 \, \mathrm{d}t}, \tag{1.12}$$

with

$$\mathcal{N} = \int \mathrm{e}^{-\frac{1}{4B}\int_{\mathbb{R}} \|\boldsymbol{\eta}\|^2 \, \mathrm{d}t} \, \mathrm{D}\boldsymbol{\eta}. \tag{1.13}$$

Remark. Usually the distribution (1.12) is not specified and the noise is characterised by its average and autocorrelation

$$\langle \eta_i(t) \rangle = 0 \tag{1.14a}$$

$$\langle \eta_i(t_1) \eta_j(t_2) \rangle = 2B \, \delta_{ij} \, \delta(t_1 - t_2). \tag{1.14b}$$

Here $\langle \cdot \rangle$ denotes the average over the probability distribution of the noise. This passage is important, since it defines the expectation value of a Langevin process.

For the sake of simplicity we focus on the overdamped case of large ζ. This passage is non trivial, since the velocity and the noise become discontinuous in time. If the particle gets a random kick at time t, its amplitude depends on the position at time t. Here we adopt the Îto convention, which means assuming that the amplitude of the kick is related to the position immediately before t [3]. Neglecting the inertial term and rescaling time as $t \mapsto \frac{t}{\zeta}$ we get

$$\dot{\boldsymbol{x}}(t) = -\boldsymbol{\nabla} V + \boldsymbol{\eta}(t). \tag{1.15}$$

Since the trajectory of the particle is itself a stochastic process, we are mainly interested in its expectation value and variance. To this end, we can formally solve (1.15) for a particular realisation of the noise process. Then, average the result using (1.14a - 1.14b).

1.3 A distribution over paths

Given a fixed noise profile $\boldsymbol{\eta}$ and initial condition $\boldsymbol{x}_0$, the trajectory of the particle is fully determined by the Langevin equation. This means that the probability that the particle takes a specific path is

$$\mathcal{P}[\boldsymbol{x}(t)] = \frac{1}{\mathcal{N}} \, \mathrm{e}^{-\frac{1}{4B}\int_{\mathbb{R}} \|\dot{\boldsymbol{x}}+\boldsymbol{\nabla} V\|^2 \, \mathrm{d}t}. \tag{1.16}$$

Rather than considering the probability distribution of the specific path, we might be interested in the probability that a particle that started in position $\boldsymbol{x}_0$ at time t_0 sits in $\boldsymbol{x}_f$ at time t, regardless of the specific trajectory. This vocabulary should sound much closer to that of equilibrium statistical mechanics, which is ultimately based on probability distributions in configuration space. The difference here is that time gets promoted to a degree of freedom. The total probability is a sum over paths satisfying the Langevin equation that start in $\boldsymbol{x}_0$ at t_0 and end $\boldsymbol{x}_f$ at t, averaged over the noise. We must also include a Jacobian $\mathcal{J}[\boldsymbol{x}]$ to count each solution with unit weight:

$$\begin{aligned} P(\boldsymbol{x}_f, t) &= \left\langle \int_{\boldsymbol{x}_i}^{\boldsymbol{x}_f} \det\left(\mathcal{J}[\boldsymbol{x}]\right) \delta[\dot{\boldsymbol{x}} + \boldsymbol{\nabla} V - \boldsymbol{\eta}] \, \mathrm{D}\boldsymbol{x} \right\rangle \\ &= \left\langle \iint \mathrm{e}^{-\int_{\mathbb{R}} \tilde{\boldsymbol{x}}\cdot(\dot{\boldsymbol{x}}+\boldsymbol{\nabla} V-\boldsymbol{\eta}) \, \mathrm{d}t} \, \mathrm{D}\tilde{\boldsymbol{x}} \, \mathrm{D}\boldsymbol{x} \right\rangle \\ &= \iint \mathrm{e}^{-\int_{\mathbb{R}} \tilde{\boldsymbol{x}}\cdot(\dot{\boldsymbol{x}}+\boldsymbol{\nabla} V-B\tilde{\boldsymbol{x}}) \, \mathrm{d}t} \, \mathrm{D}\tilde{\boldsymbol{x}} \, \mathrm{D}\boldsymbol{x}, \end{aligned} \tag{1.17}$$

where we exploited the fact that $\det\left(\mathcal{J}[\boldsymbol{x}]\right) = 1$ in the Îto convention and we used the integral representation of the delta function [6]. Rescaling $\tilde{\boldsymbol{x}} \mapsto \frac{\tilde{\boldsymbol{x}}}{B}$ we get

$$P(\boldsymbol{x}_f, t) = \iint \mathrm{e}^{-\frac{1}{B}\int_{\mathbb{R}} \tilde{\boldsymbol{x}}\cdot(\dot{\boldsymbol{x}}+\boldsymbol{\nabla} V-\tilde{\boldsymbol{x}}) \, \mathrm{d}t} \, \mathrm{D}\tilde{\boldsymbol{x}} \, \mathrm{D}\boldsymbol{x}. \tag{1.18}$$

The probability (1.18) has the form of a partition function at 'temperature' B. The probability of going from $\boldsymbol{x}_0$ at t_0 to $\boldsymbol{x}_f$ at time t is dominated by the extremal trajectories, which minimise the action

$$\mathcal{S}[\boldsymbol{x}, \tilde{\boldsymbol{x}}] = \int_{\mathbb{R}} \tilde{\boldsymbol{x}} \cdot (\dot{\boldsymbol{x}} + \boldsymbol{\nabla} V - \tilde{\boldsymbol{x}}) \, \mathrm{d}t. \tag{1.19}$$

Solutions such that

$$\begin{cases} \dot{\boldsymbol{x}} = -\boldsymbol{\nabla} V \\ \tilde{\boldsymbol{x}} = \mathbf{0}, \end{cases} \tag{1.20}$$

are the 'deterministic' trajectories that the particle would follow in the absence of noise. However, when $B > 0$, paths deviating from such trajectories become available, even if their probability is exponentially suppressed [3].

1.4 Equilibrium and time-reversal symmetry

In section 1.1.2 we discussed the connection between detailed balance and a microscopic definition of equilibrium. Here we would like to deepen this link using the tools introduced in the last section. We can imagine to telescope (1.8) over intermediate steps to write it in a more insightful form

$$\mathcal{P}[\boldsymbol{x}(t)] = \frac{P(\boldsymbol{x}_f, t)}{P(\boldsymbol{x}_0, t)} \mathcal{P}\Big[\boldsymbol{x}^{(R)}(t)\Big], \tag{1.21}$$

where $\boldsymbol{x}^{(R)}(t)$ is the reversed path from $\boldsymbol{x}_f$ to $\boldsymbol{x}_0$. This means that the probability of a path $\boldsymbol{x}(t)$ is equal to that of the reversed path times a constant that solely depends on the initial and final conditions. Stated that way, it is clear that the microscopic definition of equilibrium is deeply related to the presence of a time-reversal symmetry in the system. When this symmetry is broken, for example by the action of non-conservative forces, (1.21) is no longer satisfied and the system falls out of equilibrium [3]. Note that systems in non-equilibrium steady states still exhibit a time translation symmetry. A particular class of systems that manifestly violates detailed balance will be one of the main subjects of this thesis.

Chapter 2

Absorbing phase transitions

A phase of matter is a state of a system characterised by some of its macroscopic variables that are essentially uniform [7]. Traditionally, phases are only defined for equilibrium systems, but this notion can be extended. Consider for example an epidemic where infected individuals can transmit the disease to healthy ones at rate λ and can recover at rate μ. When $\kappa = \lambda - \mu$ is large, the disease spreads rapidly, until the fraction of infected fluctuates around a non-zero value. On the other hand, when κ is sufficiently small, infected individuals have time to recover before transmitting the disease and the epidemic comes to a halt. Therefore, the parameter κ controls a transition between an 'active phase', where the epidemic persists, and an 'inactive phase', where the system is trapped into an absorbing state. Notice that, even in the steady state, the system is always out of equilibrium as it violates the definition of detailed balance: once the dynamics reach the absorbing state through a path in configuration space, the probability of the reversed path is strictly zero, hence (1.21) no longer holds. Despite this fact, absorbing phase transitions have much in common with continuous equilibrium transitions: universality classes can be defined as well as scaling laws and critical exponents that describe the physics near the critical point that separates the two

phases. Contrary to equilibrium situations, time becomes an additional degree of freedom that needs to be considered. The critical behaviour can thus be even richer as new scaling laws describe the relaxation of the initial state as a function of time [1, 8, 9].

In this chapter, we present the general features of absorbing phase transitions by following the books by M. Henkel *et al.* [1] and by R. Livi and P. Politi [8].

2.1 General model

We consider a many-particle system governed by some stochastic dynamics. Each particle is labelled by a variable $n_i(t) \in \{0,1\}$ which tells us whether it is active (e.g. infected) or not. We define the order parameter as the fraction of active particles at time t

$$\varrho(t) = \frac{1}{N} \sum_{i=1}^{N} n_i(t). \tag{2.1}$$

In the active phase of an infinite system, ϱ reaches a constant, non-zero value, while it vanishes in the absorbing phase. In the long time limit, we expect the order parameter to vanish continuously with a power law as the control parameter κ approaches zero from above

$$\varrho(\infty) \sim \kappa^{\beta}. \tag{2.2}$$

2.1.1 Scaling properties

The stationary state is characterised by a correlation length ξ and a correlation time τ. Both of them are expected to diverge at the critical point

$$\xi \sim |\kappa|^{-\nu_\perp} \tag{2.3a}$$

$$\tau \sim |\kappa|^{-\nu_\parallel}, \tag{2.3b}$$

with different critical exponents $\nu_\perp$ and $\nu_\parallel$. The underlying anisotropy between space and time is captured by the so-called dynamical exponent $z = {}^{\nu_\parallel}/_{\nu_\perp}$, which measures how fast local perturbations spread throughout the system. The divergence of τ and ξ imply that, at criticality, the system is invariant under scale transformations of both space and time. This means that if we rescale

$$x \mapsto \ell^{-1}x, \quad t \mapsto \ell^{-z}t, \quad \kappa \mapsto \ell^{1/\nu_\perp}\kappa \tag{2.4}$$

and all the other quantities according to

$$Q\Big(\ell^{-1}x, \ell^{-z}t, \ell^{1/\nu_\perp}\kappa\Big) = \ell^{y_Q}Q(x,t,\kappa), \tag{2.5}$$

then the resulting configurations are statistically similar to the initial ones and show the same macroscopic properties. For instance, in the stationary state, the order parameter has to rescale as

$$\varrho\Big(\ell^{1/\nu_\perp}\kappa\Big) = \ell^{y_\varrho}\varrho(\kappa). \tag{2.6}$$

If we choose $\ell = \kappa^{-\nu_\perp}$ we get

$$\varrho(\kappa) = \kappa^{y_\varrho\nu_\perp}\varrho(1) \tag{2.7}$$

and comparing with (2.2) we identify $y_\varrho = {}^{\beta}/_{\nu_\perp}$.

We can use the same trick to find the dynamical scaling behaviour of ϱ as a function of time. If we rescale according to (2.4) and we choose $\ell = t^{1/z}$ we get

$$\varrho(t) \sim t^{-\alpha}, \tag{2.8}$$

with $\alpha = {}^{\beta}/_{\nu_\parallel}$.

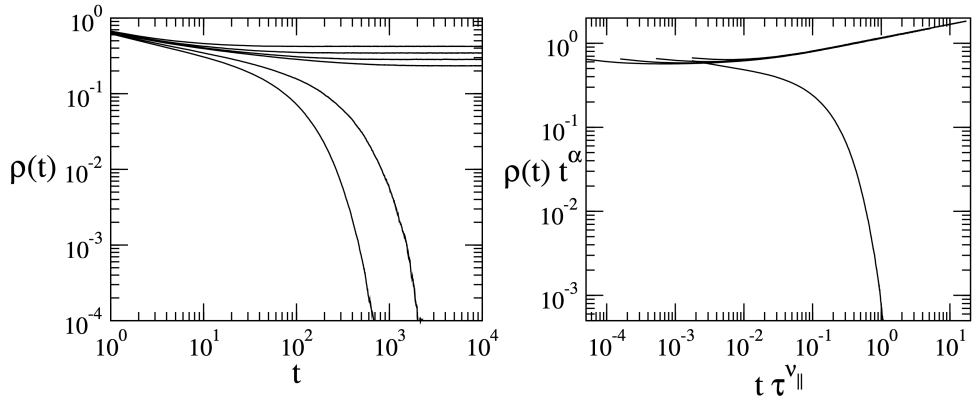

Figure 2.1: Left panel: time dependence of the order parameter for bond directed percolation starting from a fully occupied one-dimensional lattice. Right panel: data collapse obtained by rescaling the axis. Source: [1].

Another example is the correlation function

$$C(r,t,\kappa) = \langle n_1(t_1) n_2(t_2) \rangle \,, \tag{2.9}$$

where $\langle \cdot \rangle$ denotes the average over many realisations of the stochastic process and, exploiting space and time translational invariance, $r = \|\boldsymbol{r}_2 - \boldsymbol{r}_1\|$, $t = t_2 - t_1$. Applying the scale transformation (2.4)

$$C(r,t,\kappa) = \ell^{-2y_\varrho} C\Big(\ell^{-1} r, \ell^{-z} t, \ell^{1/\nu_\perp} \kappa\Big) \tag{2.10}$$

and comparing the result with the scaling form

$$C(r,t,\kappa) \sim \frac{1}{r^{d-2+\eta}}\, g_C\left(\frac{r}{\xi}, \frac{t}{\tau}\right), \tag{2.11}$$

we find

$$y_\varrho = \frac{d-2+\eta}{2}, \tag{2.12}$$

which gives the scaling law

$$\beta = \frac{d-2+\eta}{2}\, \nu_\perp. \tag{2.13}$$

2.1.2 Fluctuations

In an infinite system, the fraction of active particles reaches a stationary state with a constant value. However, if the size L of the system is finite (as in numerical simulations), the activity fluctuates around its stationary value (see figure 2.2). In particular, if $L < \xi$, finite-size effects may cause the system to reach the absorbing state after a characteristic time, even if $\kappa > 0$. If instead $L \gg \xi$, each of the $(L/\xi)^d$ uncorrelated subsystems gives an independent contribution to fluctuations of the activity, the sum of which is normally distributed. We can thus quantify fluctuations by taking the variance

$$\chi = N\Big(\big\langle \varrho^2 \big\rangle - \langle \varrho \rangle^2\Big), \tag{2.14}$$

which diverges at criticality as

$$\chi \sim |\kappa|^{-\gamma'}, \tag{2.15}$$

with

$$\gamma' = d\nu_\perp - 2\beta. \tag{2.16}$$

In equilibrium phase transitions, the variance of the order parameter is related to the response of the system to an external perturbation through the fluctuations-dissipation theorem. This is not necessarily true out of equilibrium, hence the critical exponents characterising the divergence of fluctuations and susceptibility are in general different for absorbing phase transitions.

2.2 A simple example

Let us go back to the example of an epidemic. We would like to model the spread of the disease with a phenomenological Langevin equation for the coarse-grained average of the number of infected individuals $\varrho(\boldsymbol{x}, t)$. When two individuals meet

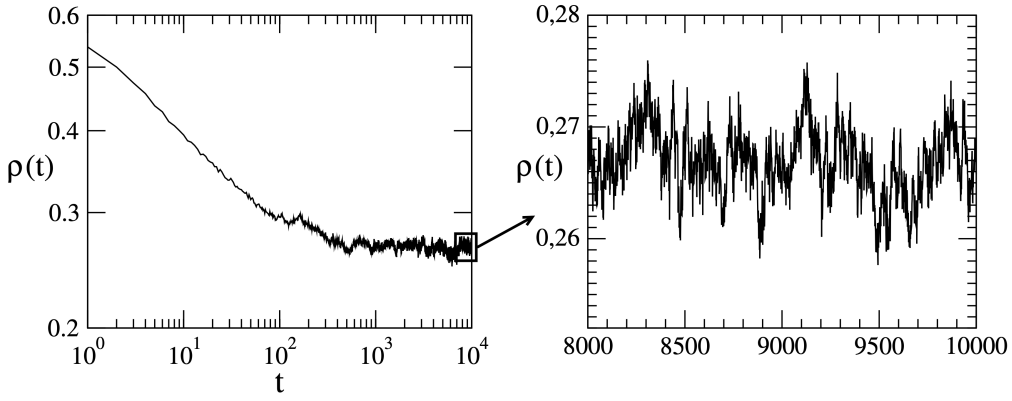

Figure 2.2: Fluctuations of the order parameter for bond directed percolation at steady state. Source: [1].

in $(\boldsymbol{x}, t)$, the infection occurs at a rate $\lambda\varrho(1-\rho)$, while the recovery rate is $\mu\varrho$. We also account for diffusive spreading by introducing a term $D\nabla^2\varrho$, so that the mean-field equation for the field $\varrho(\boldsymbol{x}, t)$ reads

$$\frac{\partial\varrho}{\partial t}(\boldsymbol{x}, t) = D\nabla^2\varrho(\boldsymbol{x}, t) + \kappa\varrho(\boldsymbol{x}, t) - \lambda\varrho^2(\boldsymbol{x}, t), \tag{2.17}$$

with $\kappa = \lambda - \mu$. The homogeneous stationary solution gives $\varrho(\infty) \sim \kappa$, which implies $\beta^{\mathrm{MF}} = 1$. Applying the scale transformation (2.4) we get the rescaled equation

$$\ell^{-z-\frac{\beta}{\nu_\perp}}\frac{\partial\varrho}{\partial t} = \ell^{-2-\frac{\beta}{\nu_\perp}}D\nabla^2\varrho + \ell^{-\frac{1}{\nu_\perp}-\frac{\beta}{\nu_\perp}}\kappa\varrho - \ell^{\frac{2\beta}{\nu_\perp}}\lambda\varrho^2, \tag{2.18}$$

which is invariant if $z^{\mathrm{MF}} = 2$, $\nu_\parallel^{\mathrm{MF}} = 1$, $\nu_\perp^{\mathrm{MF}} = 1/2$ [6].

To account for fluctuations from the average value of ϱ, we introduce a noise term that must switch off when $\varrho = 0$, to respect the absorbing state. The equation becomes

$$\frac{\partial\varrho}{\partial t}(\boldsymbol{x}, t) = D\nabla^2\varrho(\boldsymbol{x}, t) + \kappa\varrho(\boldsymbol{x}, t) - \lambda\varrho^2(\boldsymbol{x}, t) + \eta(\boldsymbol{x}, t), \tag{2.19}$$

with

$$\langle\eta(\boldsymbol{x}, t)\rangle = 0 \tag{2.20a}$$

$$\langle\eta(\boldsymbol{x}, t)\eta(\boldsymbol{x}', t')\rangle = \gamma\varrho(\boldsymbol{x}, t)\,\delta(\boldsymbol{x} - \boldsymbol{x}')\,\delta(t - t'). \tag{2.20b}$$

Equation (2.19) describes the critical behaviour of the so-called directed percolation (DP) universality class, which is the ideal example of absorbing phase transitions.

Dimensional analysis shows that the noise term is irrelevant for $d > 4$, meaning that $d_{uc} = 4$ is the upper critical dimension of DP. The system can be studied in $d < d_{uc}$ with field-theoretic renormalisation group method. Using the same procedure we described in section 1.3, we can derive the corresponding dynamic functional

$$\mathcal{S}[\varrho, \tilde{\varrho}] = \int_{\mathbb{R}^{d+1}} \tilde{\varrho}\Big(\partial_t \varrho - D\nabla^2 \varrho - \kappa\rho + \lambda\varrho^2 - \frac{\gamma}{2}\varrho\tilde{\varrho}\Big)\,\mathrm{d}\boldsymbol{x}\,\mathrm{d}t, \tag{2.21}$$

where $\tilde{\varrho}(\boldsymbol{x}, t)$ is the response field conjugated to $\eta(\boldsymbol{x}, t)$. Setting

$$\phi = \sqrt{\frac{2\lambda}{\gamma}}\,\varrho, \quad \tilde{\phi} = \sqrt{\frac{\gamma}{2\lambda}}\,\tilde{\varrho}, \quad \Gamma = 2\sqrt{\frac{\lambda\gamma}{2}}, \tag{2.22}$$

turns the functional into

$$\mathcal{S}\big[\phi, \tilde{\phi}\big] = \int_{\mathbb{R}^{d+1}} \left(\tilde{\phi}\big(\partial_t - D\nabla^2 - \kappa\big)\phi + \frac{\Gamma}{2}\big(\tilde{\phi}\phi^2 - \phi\tilde{\phi}^2\big)\right)\mathrm{d}\boldsymbol{x}\,\mathrm{d}t, \tag{2.23}$$

which correspond to the Lagrangian of the Reggeon field theory in particle physics. Critical exponents in $d < d_{uc}$ can be computed perturbatively from this functional by means of an ϵ-expansion around the upper critical dimension. This formulation reveals an important symmetry of DP, which is known as rapidity-reversal symmetry: it is easy to see that the action (2.23) is invariant under the transformation

$$\phi(\boldsymbol{x}, t) \leftrightarrow \tilde{\phi}(\boldsymbol{x}, -t). \tag{2.24}$$

This symmetry does not need to be present at the microscopic level, but it emerges at the coarse-grained scale for all models belonging to the DP class.

2.3 Universality classes

In equilibrium phase transitions, universality classes are fundamentally related to a set of symmetries that the system satisfies. A similar classification for absorbing

phase transitions is not simple, since symmetries generally emerge only at a coarse-grained level [1]. A typical example is the already mentioned rapidity-reversal symmetry in directed percolation. However, we can still identify some relevant parameters (such as the dimensionality of space and the presence of conservation laws) that can help us distinguish between universality classes [8].

2.3.1 The DP conjecture

Directed percolation represents the prototype of absorbing phase transitions. Interestingly, the choice of the microscopic dynamics used to model the DP process does not affect the critical exponents, provided that these rules involve short-ranged interaction only and do not introduce additional symmetries or conservation laws [1]. Similarly to many equilibrium models, the macroscopic critical behaviour of DP can be explained by the same coarse-grained description given by (2.23), where all irrelevant microscopic details have been averaged out. As a consequence, many processes ranging from fluids percolating through a medium to the already mentioned spread of epidemics fall in the DP universality class. According to the conjecture by Janssen [10] and Grassberger [11], any model that

- exhibits a continuous phase transition from a fluctuating active phase into a unique absorbing state,
- is described by a non-negative one-component order parameter,
- includes short-ranged dynamic rules only,
- has no unconventional symmetries, conservation laws, or quenched randomness,

should belong to the DP universality class. The robustness of the DP class seems to extend even further, as it has been found in some models with more than one absorbing states or with non-scalar order parameters [1]. Nonetheless,

universality classes different from DP appear in systems with additional symmetries and conservation laws. The estimates of some of the DP critical exponents can be found in table 2.1.

	$d = 1$	$d = 2$	$d = 3$	Mean-field
α	0.16	0.45	0.73	1
β	0.276	0.583	0.813	1
γ'	0.545	0.30	0.81	0
$\nu_\parallel$	1.734	1.295	1.11	1
$\nu_\perp$	1.097	0.733	0.584	$1/2$

Table 2.1: Critical exponents of the DP universality classes. Source: [12].

2.3.2 Conserved directed percolation

Conserved directed percolation (CDP) is a class of absorbing phase transitions where the order parameter is coupled to a non-diffusive conserved field that has an infinite number of absorbing states [1]. A typical example is a system where the number of particles is conserved. As opposed to DP, CDP is less understood and it still lacks precise quantitative results from theoretical approaches. Several attempts have been made in this direction, including path integral representations [13], series expansions [14] and an exact mapping to the continuum theory of disordered elastic interfaces [15].

The simplest model belonging to the CDP class is the so-called Manna model. In the simplest version of this model, each site of a lattice with periodic boundary conditions can be occupied by any number n of 'sand-grains'. At each discrete time step, each lattice site with $n > 1$ is labelled as active and it redistributes all of its grains among randomly chosen neighbours. By varying the particle density ρ this model undergoes an absorbing phase transition from an active phase, where the

fraction of active sites ϱ fluctuates, to an absorbing phase where $\varrho = 0$.

Table 2.2 contains estimates of the critical exponents of the CDP class. Notice that, above the upper critical dimension $d_{uc} = 4$, the two classes exhibit the same mean-field behaviour.

	$d = 1$	$d = 2$	$d = 3$	Mean-field
α	0.141(24)	0.419(15)	0.745(17)	1
β	0.38(2)	0.639(9)	0.840(12)	1
γ'	0.550(40)	0.367(19)	0.152(17)	0
$\nu_\parallel$	1.88(14)	1.225(29)	1.081(27)	1
$\nu_\perp$	1.35(9)	0.799(14)	0.593(13)	$1/2$

Table 2.2: Critical exponents of the CDP universality classes. Source: [1].

2.4 A model for sheared systems

In 2005 D.J. Pine and coworkers published the results of an experimental study of a periodically driven viscous suspension of non-Brownian particles (i.e. a suspension is made of particles that are too large to be sensitive to thermal motion) [16]. The authors showed that, by changing the shear amplitude, the system undergoes a non-equilibrium phase transition from an irreversible diffusive phase to a reversible absorbing state in which all particles return to their original position after a shear cycle [16, 17, 18].

The behaviour of a simple fluid undergoing shear at low Reynolds number Re is expected to be reversible, as the Stokes equations governing its dynamics are time reversible. The same equations are also expected to govern the dynamics of non-Brownian particles at low Re, but their motion becomes chaotic (i.e. very sensitive to initial conditions) in the creeping flow limit. While some authors attributed the emergence of irreversibility to a growth in the Lyapunov exponent,

which measures the separation of trajectories in phase space with 'close' initial conditions, numerical models identified diverging lengthscales and timescales, which are the hallmark of a dynamical phase transition [19, 20, 21].

In 2015 E. Tjhung and L. Berthier developed a numerical model for the experiments on sheared suspensions [19], by modifying a previous model by L. Corté and coworkers [17]. In both cases, the authors simplified the microscopic irreversibility due to particle collisions into a much simpler discrete stochastic model, in which overlapping particles interact through some dynamical rule.

In the model by Tjhung and Berthier (TB), they considered N spherical particles of diameter σ in a 2-dimensional box of size L with periodic boundary conditions. At each discrete time step t, if two or more particle overlap, they are given an independent random displacement $\boldsymbol{\delta}$ with amplitude δ uniformly distributed in the interval $[0, \epsilon]$ and orientation distributed on a unit circle. The maximal amplitude of the 'kicks' ϵ and the packing fraction

$$\phi = \frac{N\pi\sigma^2}{4L^2} \tag{2.25}$$

are the two control parameters of the model (figure 2.3).

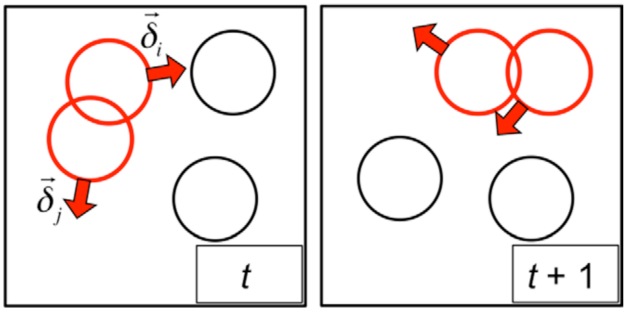

Figure 2.3: Graphical representation of the stochastic dynamical rule used in TB. Source: [19].

Intuitively, when the packing fraction is sufficiently large, overlaps will be present at each time step and particles continue to move forever. On the other hand, when

ϕ is small, the system is expected to reach an absorbing configuration with no overlaps where all particles are frozen. This model somewhat mimics the behaviour of the experimental suspension of non-Brownian particles, since giving a random kick to each particle with at least one neighbour in a region near its centre is equivalent to give a random displacement to all particles colliding during a shear cycle. The simplification introduced by the authors amounts to considering the interactive region to be a circle of diameter σ. Perhaps not surprisingly, the choice of different stochastic rules for the microscopic dynamics does not seem to change the universal behaviour observed for the original model [20, 21].

In TB, the authors reported strong evidences of an absorbing phase transition at a critical packing fraction $\phi_c(\epsilon)$, with critical exponents compatible with both DP and CDP. This was achieved by studying the critical behaviour of the order parameter (2.1) and its fluctuations (2.14), while measuring both static and dynamic correlation lengths and several independent timescales. The results are summarised in figure 2.4 and in table 2.3. All these quantities are accessible in experiments and can be used to study the irreversibility transition in non-Brownian suspensions.

	TB	DP	CDP
α	0.45	0.45	0.42
β	0.59(2)	0.58	0.64
γ'	0.32(2)	0.30	0.37
$\nu_\parallel$	1.26(3)	1.30	1.23
$\nu_\perp$	0.74(3)	0.73	0.8

Table 2.3: Critical exponents of the TB model compared to the DP and CDP universality classes in two dimensions. Source: [19].

Additionally, configurations at the critical point were found to be hyperuniform, i.e. they exhibit anomalously small density fluctuations [22]. More specifically, a system with volume L^d is hyperuniform if the variance of the total number of

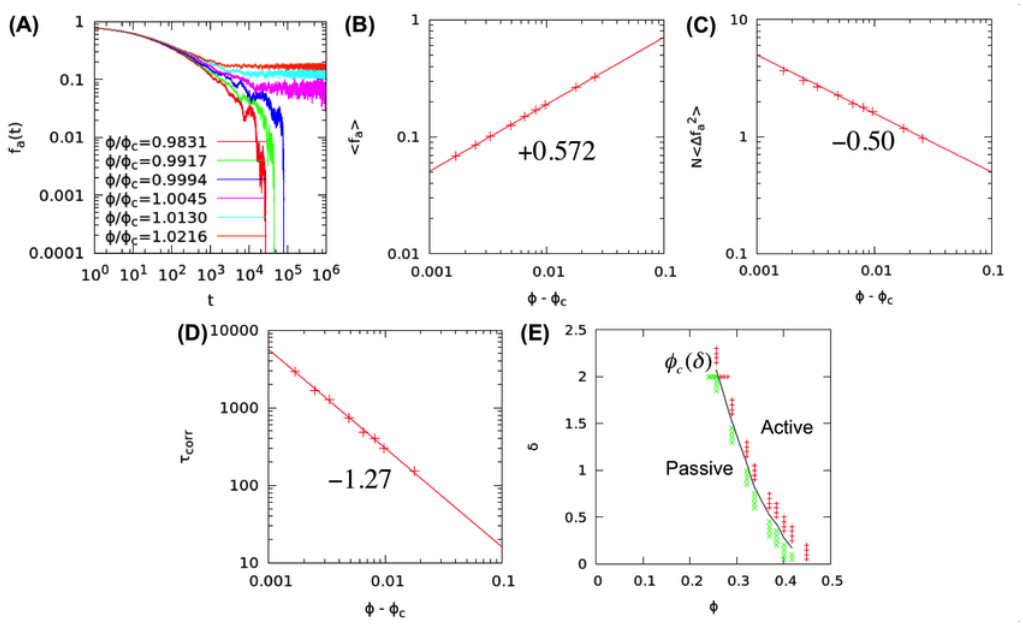

Figure 2.4: (A) Time dependence of the order parameter. (B-D) Critical scaling of the order parameter, fluctuations at steady state and correlation time. (D) Phase diagram in the (ϕ, ϵ) plane. Source: [19].

particles

$$\left\langle \delta N^2 \right\rangle = \left\langle N^2 \right\rangle - \langle N \rangle^2 \tag{2.26}$$

scales as

$$\left\langle \delta N^2 \right\rangle \sim L^{d-\lambda}. \tag{2.27}$$

The authors measured the value $\lambda = 1$ for their model at criticality, which corresponds to that of a periodic lattice. Away from the critical point, hyperuniform scaling holds up to a lengthscale ℓ_H, which diverges at criticality with an exponent different from that of the correlation length (figure 2.5). This means that there are no clear connections between fluctuations of the activity and hyperuniform fluctuations.

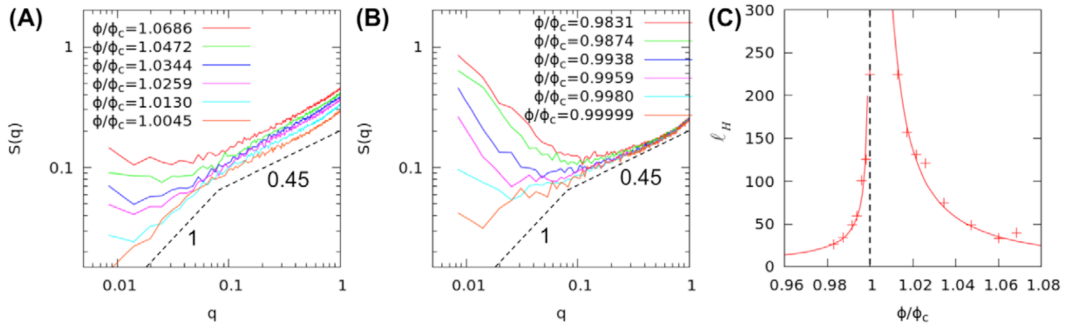

Figure 2.5: (A) Structure factor for different packing fractions $\phi > \phi_c$. (B) Structure factor for $\phi < \phi_c$. (C) Divergence of the hyperuniform lengthscale ℓ_H. Source: [19].

Chapter 3

Two dimensional solids

We are very familiar with the solid state, which is one of the fundamental states of matter. The constituents of a solid are generally packed together much closer than particles in a fluid, which results in a much larger mechanical rigidity than that of a liquid [23]. Based on the local arrangement of their particles, solids can be distinguished into [24]

- amorphous solids, characterised by the absence of periodicity and any form of long-range order,
- quasi-crystals, made of non-periodic but regular arrangement of constituents,
- crystalline solids, that are infinite periodic structures with long-range positional and orientational order.

In this chapter, we briefly discuss the harmonic theory of crystalline solids and we introduce some observables that are useful to quantify the degree of order in a solid. Since (thermal) fluctuations tend to destroy the order of a system (think for example of the Ising model in one dimension), we could ask ourselves whether a crystalline solid is a stable phase at finite temperature. We will see that, at

thermal equilibrium, the stability of a crystal depends on the dimensionality of the system. We will then introduce the notion of topological defects in ordered media and discuss their role in the relaxation process of a system towards its steady state. Finally, we will give a brief introduction to the liquid-solid transition in two dimensions.

This chapter is largely influenced by the thesis of Juliane Klamser [25] and by the lecture notes of Leticia Cugliandolo *et al.* [26].

3.1 Harmonic approximation

One of the simplest models for a crystalline solid is that of an arrangement of N spheres of mass m in d dimensions connected by ideal springs [27] (figure 3.1). These springs are at rest when each sphere occupies its equilibrium position $\boldsymbol{r}_i^0$, that corresponds to a lattice site in the periodic arrangement of the crystal. At finite temperature, the spheres oscillate around their site and their time-dependent position can be written as

$$\boldsymbol{r}_i(t) = \boldsymbol{r}_i^0 + \boldsymbol{u}_i(t), \tag{3.1}$$

where $\boldsymbol{u}_i$ is the displacement of particle i around its lattice site. The Hamiltonian of the model reads

$$\mathcal{H} = \sum_i \frac{p_i^2}{2m} + U(\{\boldsymbol{r}_i\}), \tag{3.2}$$

where

$$U(\{\boldsymbol{r}_i\}) = \sum_{i<j} V(\boldsymbol{r}_i - \boldsymbol{r}_j) \tag{3.3}$$

is the interaction potential that has a minimum in the equilibrium configuration.

Assuming that $\|\boldsymbol{u}_i\| \ll a$, where a is the lattice spacing, we can expand the potential around its minimum

$$U(\{\boldsymbol{r}_i\}) \approx U\Big(\big\{\boldsymbol{r}_i^0\big\}\Big) + \frac{1}{2}\sum_{\alpha,\beta}\sum_{i,j} K_{i\alpha}^{j\beta} u_{i\alpha} u_{j\beta}, \tag{3.4}$$

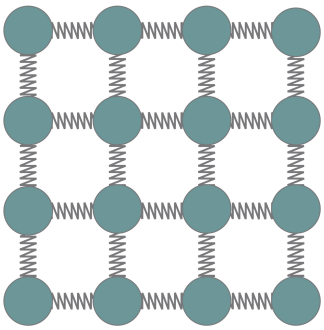

Figure 3.1: Schematic representation of a two-dimensional harmonic solid on a square lattice. Source: [25].

where

$$K_{i\alpha}^{j\beta} = \left.\frac{\partial^2 U}{\partial u_{i\alpha} u_{j\beta}}\right|_{\substack{u_{i\alpha}=0 \\ u_{j\beta}=0}} \tag{3.5}$$

represent the elastic constant of the spring connecting particle i with particle j.

The equations of motion for the displacements $\boldsymbol{u}_i$

$$m\ddot{u}_{i\alpha} = -\sum_{j,\beta} K_{i\alpha}^{j\beta} u_{j\beta} \tag{3.6}$$

form a system of dN coupled differential equations. To solve it, we introduce the Fourier representation of the displacements

$$\boldsymbol{u}_i(t) = \frac{1}{\sqrt{N}} \sum_{\boldsymbol{q}} \hat{\boldsymbol{u}}_{\boldsymbol{q}}(t)\, \mathrm{e}^{\mathrm{i}\boldsymbol{q}\cdot\boldsymbol{r}_i^0}, \tag{3.7}$$

with

$$\hat{\boldsymbol{u}}_{\boldsymbol{q}}(t) = \mathrm{e}^{-\mathrm{i}\omega_{\boldsymbol{q}} t} \boldsymbol{e}_{\boldsymbol{q}}. \tag{3.8}$$

Substituting into (3.6) and exploiting orthogonality of plane waves we get

$$\omega_{\boldsymbol{q}}^2 e_{\boldsymbol{q}\alpha} = \sum_{\beta} D_{\alpha}^{\beta}(\boldsymbol{q}) e_{\boldsymbol{q}\beta}, \tag{3.9}$$

where

$$D_{\alpha}^{\beta}(\boldsymbol{q}) = \frac{1}{m} \sum_{\ell} K_{0\alpha}^{\ell\beta}\, \mathrm{e}^{\mathrm{i}\boldsymbol{q}\cdot\boldsymbol{r}_\ell^0} \tag{3.10}$$

are the elements of the so-called dynamical matrix. The problem has been simplified to a system of algebraic linear equation decoupled in $\boldsymbol{q}$. For each $\boldsymbol{q}$, (3.9) has d solutions corresponding to the eigenvalues $\omega_{\boldsymbol{q}}^s$ and eigenvectors $\boldsymbol{e}_{\boldsymbol{q}}^s$ of the dynamical matrix $\mathsf{D}(\boldsymbol{q}) \in \mathbb{C}^{d\times d}$. The general solution is given by a superposition of all modes

$$\hat{u}_{\boldsymbol{q}\alpha}(t) = \sum_s c_{\boldsymbol{q}}^s e_{\boldsymbol{q}\alpha}^s \, \mathrm{e}^{-\mathrm{i}\omega_{\boldsymbol{q}} t}, \tag{3.11}$$

with expansion coefficients $c_{\boldsymbol{q}}^s$. The displacement of each atom can thus be written as

$$u_\alpha(t) = \frac{1}{\sqrt{N}} \sum_{s,\boldsymbol{q}} c_{\boldsymbol{q}}^s e_{\boldsymbol{q}\alpha}^s \, \mathrm{e}^{\mathrm{i}\left(\boldsymbol{q}\cdot\boldsymbol{r}_i^0 - \omega_{\boldsymbol{q}} t\right)}, \tag{3.12}$$

that is a superposition of Fourier components oscillating at frequency $\omega_{\boldsymbol{q}}$.

3.2 Stability of the crystal

To check whether the infinite periodic crystal is stable with respect to thermal fluctuations, we introduce the mean squared displacement (MSD)

$$\mathrm{MSD}(t) = \frac{1}{N} \sum_i \left\langle \|\boldsymbol{u}_i(t)\|^2 \right\rangle. \tag{3.13}$$

If the MSD diverges in the long time limit, then particles can move far away from their equilibrium positions, which means that the crystal is in fact not stable. We can rewrite the MSD using (3.7) as

$$\begin{aligned}
\mathrm{MSD}(t) &= \frac{1}{N^2} \sum_\alpha \sum_i \sum_{\boldsymbol{q},\boldsymbol{q}'} \left\langle \hat{u}_{\boldsymbol{q}\alpha}(t)\, \hat{u}_{\boldsymbol{q}'\alpha}(t)\, \mathrm{e}^{\mathrm{i}\boldsymbol{r}_i^0\cdot(\boldsymbol{q}+\boldsymbol{q}')} \right\rangle \\
&= \frac{1}{N} \sum_{\boldsymbol{q}} \left\langle \hat{\boldsymbol{u}}_{\boldsymbol{q}}(t) \cdot \hat{\boldsymbol{u}}_{-\boldsymbol{q}}(t) \right\rangle \\
&\sim \int_{\frac{2\pi}{L}}^{\Lambda} q^{d-1} \left\langle |\hat{\boldsymbol{u}}(\boldsymbol{q},t)|^2 \right\rangle \mathrm{d}q,
\end{aligned} \tag{3.14}$$

where we exploited orthogonality of plane waves and we introduced a continuous representation with a momentum cut-off $\Lambda \sim \frac{1}{a}$. Due to the equipartition theorem

at equilibrium, the average energy per mode is

$$\left\langle \frac{1}{2}\,\omega^2(\boldsymbol{q})\,|\hat{\boldsymbol{u}}(\boldsymbol{q})|^2 \right\rangle = \frac{k_B T}{2}, \tag{3.15}$$

which means

$$\left\langle |\hat{\boldsymbol{u}}(\boldsymbol{q})|^2 \right\rangle = \frac{k_B T}{\omega^2(\boldsymbol{q})}. \tag{3.16}$$

For small q we can use the Debye approximation $\omega(\boldsymbol{q}) \propto q$, which gives

$$\left\langle |\hat{\boldsymbol{u}}(\boldsymbol{q})|^2 \right\rangle \sim \frac{1}{q^2} \tag{3.17}$$

and finally, for $L \to +\infty$,

$$\mathrm{MSD}(\infty) \sim \begin{cases} L^{2-d}, & d < 2 \\ \ln(L), & d = 2 \\ \text{const}, & d > 2. \end{cases} \tag{3.18}$$

The MSD diverges if $d \leq 2$, which means that the periodic crystal is not stable in two dimensions at equilibrium. This is a direct consequence of the Mermin-Wagner theorem [28]. Nonetheless, since all particles are still centered around lattice sites, the system is still a solid with non-zero shear modulus.

Despite lacking long-range translational order, a two-dimensional harmonic solid can still have long-range orientational order [29, 30]. To see this, we introduce the orientation field

$$\boldsymbol{\phi}(\boldsymbol{R}) = \boldsymbol{r}(\boldsymbol{R} + \boldsymbol{a}) - \boldsymbol{r}(\boldsymbol{R}), \tag{3.19}$$

where $\boldsymbol{R}$ denotes a lattice site and $\boldsymbol{a}$ is a lattice vector. Since

$$\left\langle \Big(\boldsymbol{u}(\boldsymbol{R} + \boldsymbol{a}) - \boldsymbol{u}(\boldsymbol{R})\Big) \cdot \Big(\boldsymbol{u}(\boldsymbol{R}' + \boldsymbol{a}) - \boldsymbol{u}(\boldsymbol{R}')\Big) \right\rangle \to 0, \tag{3.20}$$

for $\|\boldsymbol{R} - \boldsymbol{R}'\| \to +\infty$, it is easy to see that,

$$\langle \boldsymbol{\phi}(\boldsymbol{R}) \cdot \boldsymbol{\phi}(\boldsymbol{R}') \rangle \to a^2, \quad \|\boldsymbol{R} - \boldsymbol{R}'\| \to +\infty, \tag{3.21}$$

which means that correlations of the orientational field extend to the whole system.

3.3 Order in two dimensions

The positional order can be monitored through the density field

$$\rho(\boldsymbol{r}) = \frac{1}{N}\sum_{i=1}^{N}\delta(\boldsymbol{r}-\boldsymbol{r}_i) \tag{3.22}$$

and the pair correlation function

$$g(r) = \frac{1}{N\rho}\left\langle\sum_{i\neq j}\delta(\boldsymbol{r}-\boldsymbol{r}_j+\boldsymbol{r}_i)\right\rangle, \tag{3.23}$$

where $\rho = N/L^d$. The physical interpretation of $g(r)$ is that $S_{d-1}r^{d-1}\rho\, g(r)\,\mathrm{d}r$ is the average number of particles within the interval $[r,\, r+\mathrm{d}r]$ from a reference particle [31], where S_d is the surface of a d-dimensional sphere. The pair correlation function of a crystalline solid exhibits discrete peaks at distances corresponding to the lattice sites up to $r \to +\infty$. Instead, for a non periodic structure, $g(r) \to 1$ as $r \to +\infty$. In particular, the envelope of the pair correlation function of a liquid is expected to decay exponentially at large distances, while in a two-dimensional harmonic solid it decays as a power law. For this reason, the two-dimensional harmonic solid is said to be characterised by quasi-long-range translational order [32, 33].

The Fourier components of the microscopic particle density

$$\rho(\boldsymbol{q}) = \sum_{i=1}^{N}\mathrm{e}^{-\mathrm{i}\boldsymbol{q}\cdot\boldsymbol{r}_i} \tag{3.24}$$

can be used to define the structure factor

$$S(\boldsymbol{q}) = \frac{1}{N}\left\langle\rho(\boldsymbol{q})\rho(-\boldsymbol{q})\right\rangle. \tag{3.25}$$

It is easy to see that, for homogeneous systems,

$$S(\boldsymbol{q}) = 1 + \rho\int_{L^d} g(r)\,\mathrm{e}^{-\mathrm{i}\boldsymbol{q}\cdot\boldsymbol{r}}\,\mathrm{d}\boldsymbol{r}. \tag{3.26}$$

This means that $S(\boldsymbol{q})$ and $g(r)$ encode the same information, but sometimes it is convenient to study one rather than the other [34]. The structure factor can be measured experimentally by neutron or X-ray scattering techniques.

To quantify orientational order in two dimensions we introduce the quantity

$$\psi_6(\boldsymbol{r}_i) = \frac{1}{|\partial i|} \sum_{j \in \partial i} \mathrm{e}^{6\mathrm{i}\theta_{ij}}, \tag{3.27}$$

where ∂i is the set of neighbours of particle i and θ_{ij} is the angle formed by the line that links particle i and particle j with a reference axis. To determine ∂i we resort to the Voronoi tessellation. This is done by partitioning space into regions (called Voronoi cells) made of all points in the plane closer to the center of a given particle than to any other. This way the number of edges of the region enclosing particle i corresponds to the number of neighbours $|\partial i|$ of particle i [26].

The phase of $\psi_6(\boldsymbol{r}_i)$ measures the local orientation of the cell enclosing particle i. We can then define the bond-orientational order parameter

$$\Psi_6 = \frac{1}{N} \left| \sum_{i=1}^{N} \psi_6(\boldsymbol{r}_i) \right|, \tag{3.28}$$

which quantifies the global order of the solid. In a perfectly ordered solid, particles arrange on the sites of a hexagonal lattice (see figure 3.2), so that $\Psi_6 = 1$.

To monitor the correlations of the orientational order across the system we define the bond-orientational correlation function

$$g_6(r) = \frac{1}{N\rho} \left\langle \sum_{i \neq j} \psi_6(\boldsymbol{r}_i) \psi_6^*(\boldsymbol{r}_j)\, \delta(\boldsymbol{r} - \boldsymbol{r}_j + \boldsymbol{r}_i) \right\rangle. \tag{3.29}$$

The envelope of $g_6(r)$ is expected to decay exponentially in a liquid and to approach a constant in a solid with long-range orientational order [32].

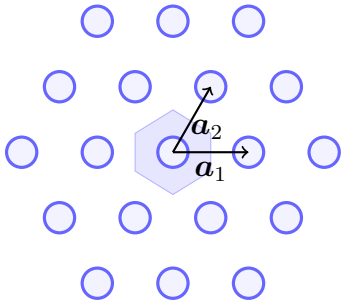

Figure 3.2: Hexagonal lattice with basis vectors $\boldsymbol{a}_1 = a(1,0)$ and $\boldsymbol{a}_2 = a\left(1/2, \sqrt{3}/2\right)$.

3.4 Topological defects

Topological defects are regions of space where the order parameter has a singular behaviour that influences the medium at large distances [35, 36]. In continuous media, a topological defect arises whenever a differential equation for the order parameter has boundary conditions that lead to homotopically distinct solutions. Two solutions are homotopically equivalent if there exists a continuous deformation, called homotopy, that can transform one into the other [35]. More formally, given a topological space X and two loops $\gamma_1, \gamma_2 \in [0,1] \to X$, such that

$$\gamma_1(0) = \gamma_2(0) = \gamma_1(1) = \gamma_2(1) = x_0, \tag{3.30}$$

a homotopy is a continuous function $F : [0,1]^2 \to X$ such that

$$F_0(s) = \gamma_1(s), \qquad \forall s \in [0,1] \tag{3.31a}$$

$$F_1(s) = \gamma_2(s), \qquad \forall s \in [0,1] \tag{3.31b}$$

$$F_t(s) = F_t(1) = x_0, \qquad \forall t \in [0,1]. \tag{3.31c}$$

Defects can be detected and classified by determining the class of an n-loop of arbitrary size around the defect itself [35]. The simplest example of topological defect is the domain wall, which can move and bend but cannot be removed by

local rearrangements of the order parameter. More complex defects arise when we consider multiple component order parameters [37] (see figure 3.3).

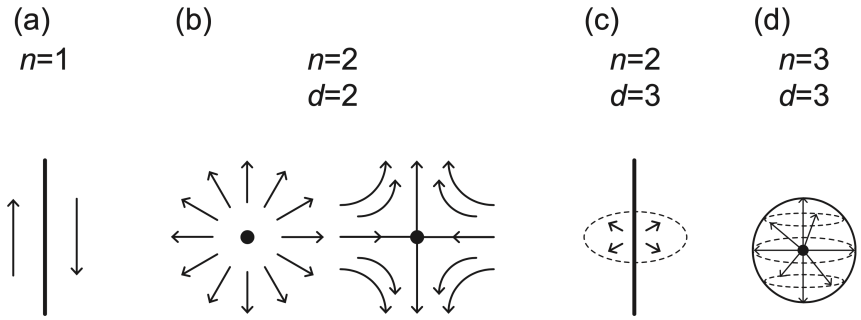

Figure 3.3: Topological defects in the $O(n)$ models. Source: [8].

3.4.1 Defects in the harmonic solid

In ordered media with broken translational symmetry and a notion of both positional and orientational order, topological defects are mis-coordinated particles with respect to the periodic lattice [38]. The most important classes of defects in a two-dimensional solid are:

- **disclinations:** They are defects generated by an isolated particle with either 5 or 7 neighbours (figure 3.4). The winding number of a disclination defines its topological charge. The phase of ψ_6 winds by -2π for a 5-disclination and by 2π for a 7-disclination, hence 5-disclinations and 7-disclinations have opposite charges. A free disclination destroys both positional and orientational order. This means that if free disclinations are stable, the system is in the disordered liquid phase.

- **dislocations:** They are pairs of disclinations with opposite charges, similarly to vortex-antivortex pairs in the two-dimensional XY model (figure 3.5). The topological charge of a dislocation is determined by the direction of the Burgers vector $\boldsymbol{b}$, which connects the two endpoints of a path that fails to close around

the defect. Free dislocations destroy positional order but preserve orientational order. When two dislocations with opposite charges form a pair, they can be enclosed by a loop with $\boldsymbol{b} = \mathbf{0}$. The resulting configuration preserves positional order away from the defect.

The interaction between defects in these two classes is the main mechanism driving the ordering transition of a two-dimensional solid in the Berezinskii-Kosterlitz-Thouless-Halperin-Nelson-Young (BKTHNY) theory, as we will briefly discuss in section 3.5.

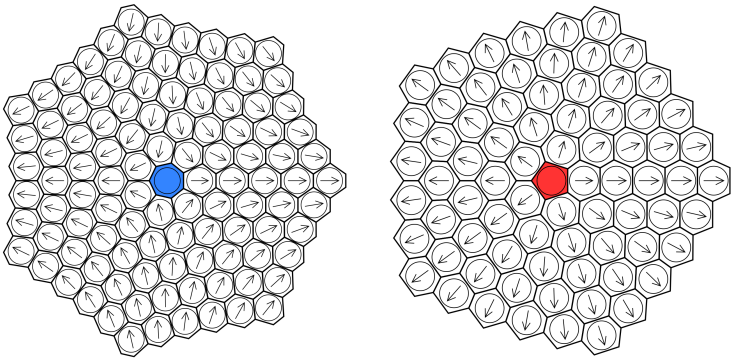

Figure 3.4: Disclinations in a hard-disk system. Source: [39].

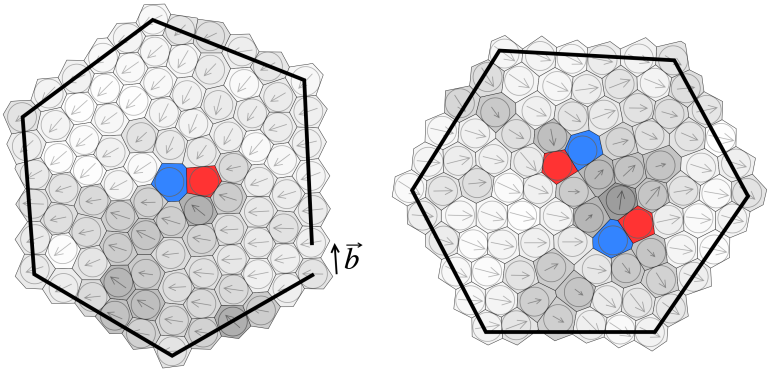

Figure 3.5: Dislocations in a hard-disk system. Source: [39].

3.4.2 Defects and coarsening

Topological defects play a fundamental role in the relaxation process of a system from an initial configuration towards its equilibrium state. Suppose to quench (i.e. rapidly change one of the control parameters) a system across a phase transition, for example by quickly cooling a paramagnet below its critical temperature. In this scenario, the initial state is no longer the equilibrium one, so the system will undergo some non-equilibrium dynamics to reach the new equilibrium point. In the late stage of the process, the dynamics develop universal features that solely depend on very general properties of the system, such as its distinctive symmetries and the number of components of the order parameter. Perhaps not surprisingly, the emergence of universality is fundamentally related to the growth of a typical length scale $R(t)$, which can be associated with the typical size of domains of the stable phase. If a system is quenched to $T < T_c$, $R(t)$ first grows up to the correlation length ξ, then it continues to grow as a power law

$$R(t) \sim t^{1/z_d}, \tag{3.32}$$

becoming the only relevant scale of the process. We will see that we can derive the coarsening law for $R(t)$ by studying the energy dissipation associated to the interactions of topological defects. For the sake of clarity, we briefly discuss the case of continuous $O(n)$ models following [8], but most of the results can be extended to systems with broken translational symmetry.

Inspired by section 1.2, we introduce a phenomenological equation of motion for the order parameter field $\boldsymbol{\phi}(\boldsymbol{x}, t)$ to describe the relaxation process in the free energy landscape with potential

$$V(\boldsymbol{\phi}) = V_0\Big(1 - \|\boldsymbol{\phi}\|^2\Big)^2, \tag{3.33}$$

so that the dynamics minimise the coarse-grained free energy functional

$$\mathcal{F}[\boldsymbol{\phi}] = \int_{\mathbb{R}^d} \left(\frac{1}{2}\|\boldsymbol{\nabla}\boldsymbol{\phi}\|^2 + V(\boldsymbol{\phi})\right) \mathrm{d}\boldsymbol{x}. \tag{3.34}$$

A reasonable generalisation of (1.15) is

$$\frac{\partial \phi_\alpha}{\partial t}(\boldsymbol{x}, t) = -\Gamma \frac{\delta F}{\delta \phi_\alpha} + \eta_\alpha(\boldsymbol{x}, t), \tag{3.35}$$

where Γ is an operator that depends on the conservation laws of the order parameter and $\boldsymbol{\eta}$ is a Gaussian noise such that

$$\langle \eta_\alpha(\boldsymbol{x}, t) \rangle = 0 \tag{3.36a}$$

$$\langle \eta_\alpha(\boldsymbol{x}, t) \eta_\beta(\boldsymbol{x}', t') \rangle = 2D\,\Gamma\,\delta_{\alpha\beta}\,\delta(\boldsymbol{x} - \boldsymbol{x}')\,\delta(t - t'). \tag{3.36b}$$

A detailed analysis of (3.35) requires perturbative renormalisation group techniques. Here we focus on a mean-field phenomenological description, which neglects the effects of thermal fluctuations encoded by the noise. For simplicity, we consider the case of a non-conserved order parameter (model A), which means setting Γ to a positive constant Γ_0 [40].

To investigate the influence of topological defects on the dynamics, we look for time-independent, radially symmetric solutions of (3.35) in the absence of noise

$$\nabla^2 \phi_\alpha = \frac{\partial V}{\partial \phi_\alpha}, \tag{3.37}$$

with $\boldsymbol{\phi}(\boldsymbol{r}) = f(r)\,\hat{\boldsymbol{u}}_r$ and boundary conditions $f(0) = 0$, $f(\infty) = 1$. Exploiting rotational symmetry, we can reduce (3.37) to the ordinary differential equation

$$f''(r) + \frac{n-1}{r} f'(r) - \frac{n-1}{r^2} f(r) = V'(f). \tag{3.38}$$

For $n = 1$, (3.38) describes a domain wall between two phases in a system with Z_2 symmetry, while for $n > 1$, it gives the profile for a general radially symmetric defect.

If $d \geq n$, the energy of the defect per unit volume in the $d-n$ dimensional space orthogonal to the core is

$$\gamma_n = \int_{L^n} \left(\frac{1}{2} \|\boldsymbol{\nabla}\boldsymbol{\phi}\|^2 + V(\boldsymbol{\phi}) \right) \mathrm{d}\boldsymbol{x}. \tag{3.39}$$

Integrating over angular variables we get

$$\gamma_n \propto \begin{cases} \text{const}, & n = 1 \\ \ln\left(\frac{L}{\xi}\right), & n = 2 \\ L^{n-2}, & n > 2. \end{cases} \tag{3.40}$$

Because of translational invariance in the $d-n$ dimensions orthogonal to the defect core, the total energy E_{def} of the defect is just $L^{d-n}\gamma_n$. When defects are not isolated we need to replace L with $R(t)$, which is the only relevant lengthscale of the system

$$E_{\text{def}} \propto \begin{cases} (R(t))^{d-1}, & n = 1 \\ (R(t))^{d-2} \ln\left(\frac{R(t)}{\xi}\right), & n = 2 \\ (R(t))^{d-2}, & n > 2. \end{cases} \tag{3.41}$$

Since the relaxation process is driven by energy dissipation, we write

$$\dot{E}_{\text{def}}(t) = \frac{\mathrm{d}E_{\text{def}}}{\mathrm{d}R}\,\dot{R}(t). \tag{3.42}$$

We can rearrange terms in (3.42) to get

$$\dot{R}(t) = -\frac{1}{\gamma_n (R(t))^{d-n}} \frac{\mathrm{d}}{\mathrm{d}R}\Big(\gamma_n (R(t))^{d-n}\Big). \tag{3.43}$$

We can then extract the scaling relation for $R(t)$ in the different cases

$$R(t) \sim \begin{cases} t^{1/2}, & d > n = 1 \\ \left(\frac{t}{\ln t}\right)^{1/2}, & d = n = 2 \\ t^{1/2}, & d > n = 2 \\ t^{1/2}, & d \geq n \geq 2. \end{cases} \tag{3.44}$$

The coarsening law can be generalised to the case of locally-conserved order parameter (model B) as well as to other models with similar defect structures [41].

3.5 Liquid-solid transition in two dimensions

We have already argued that a solid with long-range orientational order and quasi-long range positional order can exist in two dimensions. Interestingly, this solid can form from a disordered liquid state in a way that is very different from crystallisation in three dimensions, which is known to be a discontinuous transition. It is now established [42] that the ordering transition of interacting planar disks occurs in two steps: a (weakly) discontinuous transition from liquid to hexatic phase, with quasi-long range orientational order and short-range positional order, followed by a continuous transition from hexatic to solid phase. Many numerical studies [26, 43, 44] confirmed that the nature of the transitions depends on the softness of the interaction. However, given the weak discontinuous nature of the liquid-hexatic transition, it is reasonable to study the whole process in the BKTHNY scenario, suggested by B. Halperin, D. R. Nelson and P. Young in 1979 [45, 46]. This kind of transition, originally proposed by V. Berezinskii, J. M. Kosterlitz and D. J. Thouless for the two-dimensional XY model in the early 1970s, is not related to spontaneous symmetry breaking, but it is driven by the stability of topological defects above a critical temperature [47].

According to the BKTHNY theory, the disordered liquid state is characterised by the presence of free disclinations in the sytem, that destroy both positional and orientational order. As the temperature is lowered, disclinations pair into dislocations, that preserve orientational order, as described in section 3.4.1. This identifies the hexatic phase. By further reducing the temperature, pairs of dislocations with opposite charges bound together, building a solid with quasi-long-range positional order [26, 32].

Chapter 4

Random organisation at high densities

The following two chapters are dedicated to the main part of this thesis and contain the results of extensive numerical simulations and data analysis performed at the Laboratoire Charles Coulomb in Montpellier. In this chapter, we introduce the main features of our model and we discuss its absorbing phase transition in detail.

4.1 Motivation

In 2021, S. Wilken *et al.* modified the model by Tjhung and Berthier (TB) to push the critical packing fraction to high values, without affecting the universality class [20]. Interestingly, the configurations obtained for a bidisperse mixture of particle sizes seem to be structurally identical to maximally random jammed (MRJ) configurations (i.e. configurations that minimise some scalar order metric, subject to the jamming constraint [48]).

Since monodisperse spherical particles easily crystallise [34, 32], it is natural to ask whether by removing polydispersity, the model can generate ordered crystalline

configurations. This question became even more relevant when, in March 2022, Ghosh and coworkers studied a mono-layer of frictional granular disks under the influence of oscillatory shear [49] (figure 4.1).

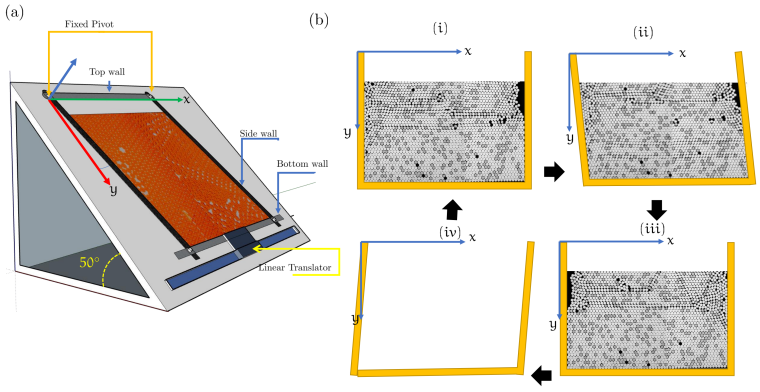

Figure 4.1: Experimental setup in the paper by Gosh *et al.* Source: [49].

The authors reported two dynamical phase transitions in their system:

- an absorbing phase transition from an active state, where disks do not return to their initial position after a shear cycle, to a an absorbing reversible state (similar to the transition described in section 2.4)

- an additional ordering transition from a disordered state to an ordered crystalline state.

The two transitions are found to take place at the same critical value of the shear amplitude, as shown by the singular behaviour of the two order parameters characterising the transitions.

Interestingly, the authors measured a set of critical exponents that are very different from those of both directed percolation (DP) and conserved directed percolation (CDP), claiming that this discrepancy could be explained by the interplay between crystallisation and the absorbing phase transition.

One of the main goals of this thesis is to build a numerical model for this experimental system and to (in)validate and help interpret the experimental observations. We have adapted the Tjhung-Berthier model in order to achieve crystallisation and measured quantities relevant for the two dynamical phase transitions.

4.2 Methods

We consider a variant of the model by Tjhung-Berthier [19]. We generate random configurations of N particles of diameter σ in a 2-dimensional box of size L with periodic boundary conditions, so that the packing fraction of the particles is

$$\phi = \frac{N\pi\sigma^2}{4L^2}. \tag{4.1}$$

At each discrete time step t, if two particles overlap, their are given opposite displacements $\boldsymbol{\delta}$ and $-\boldsymbol{\delta}$ aligned along the axis connecting their centers so that particles eventually move away from each other. The amplitude $\|\boldsymbol{\delta}\|$ of the displacement is a random number uniformly distributed in the interval $[0, \epsilon]$. If a particle overlaps with two or more neighbours, the total displacement is the sum of the contributions from each pairwise interaction. Notice that this microscopic rule conserves the center of mass of the interacting particles (figure 4.2).

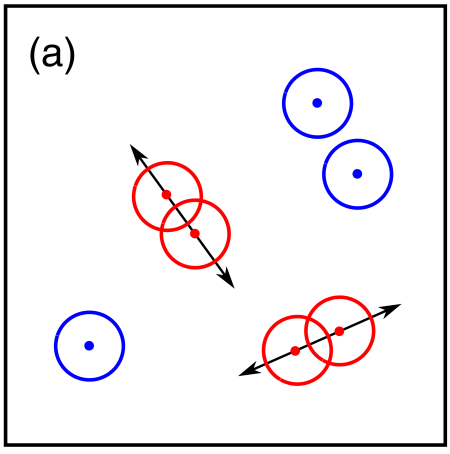

Figure 4.2: Graphical representation of the dynamical rule. Source: [50].

To reproduce the experimental results of Ghosh et al. [49], we tuned ϵ to be sufficiently small ($\epsilon = 0.1$) so that the critical packing fraction ϕ_c falls in a range where Brownian particles would typically organise in an ordered crystalline state ($\phi_c \approx 0.83$). This behaviour is very different from the one investigated by Tjhung and Berthier, where smaller packing fractions are explored dynamically and lead to disordered states only.

To check for overlaps, we keep a list of neighbours of each particle which is updated at regular intervals, so that the algorithm does not check through all particles at each simulation step. We implement this method through a custom version of the linked-list cell algorithm, the computational time of which scales as $O(N)$ for N particles [51, 52].

We run many independent simulations for different values of the control parameters ϕ and ϵ and for different system sizes. To precisely adjust the packing fraction we fix the number of particles and we change the length of the box.

We measure several physical quantities from each simulation, such as the order parameter at steady state and its fluctuations, the bond orientational order parameter, the density of topological defects, the mean-squared displacement, the pair correlation function and the structure factors in reciprocal space.

The code for the whole project has been written from scratch using the Julia programming language, with particular regard to performance and efficiency. Julia combines the high performance of compiled languages with the rapid development of the dynamic ones. This is achieved by compiling the code 'just ahead of time' before running it [53]. Access to local computer resources (a large Linux cluster) at the Laboratoire Charles Coulomb makes it possible to run simulations for very long times and allows to investigate different regions of the parameter space in parallel.

The main Julia code for the simulations is available on GitHub at this link.

4.3 Analysis of the absorbing transition

Our model exhibits an absorbing phase transition from an active state, where overlaps are present at each time step and the fraction of active particles ϱ fluctuates indefinitely, to an absorbing state where all particles are frozen.

Figure 4.3 shows two snapshots of a system with approximately 2650 particles. The typical separation between clusters of active particles can be used to define a (static) correlation length ξ for the model, as in the original work [19]. The correlation length increases approaching the critical density from above and is expected to diverge at the critical point, as we discussed in section 2.1.1. The two snapshots are taken from supplementary movies 1 and 2, which track the activity of the particles at each time step.

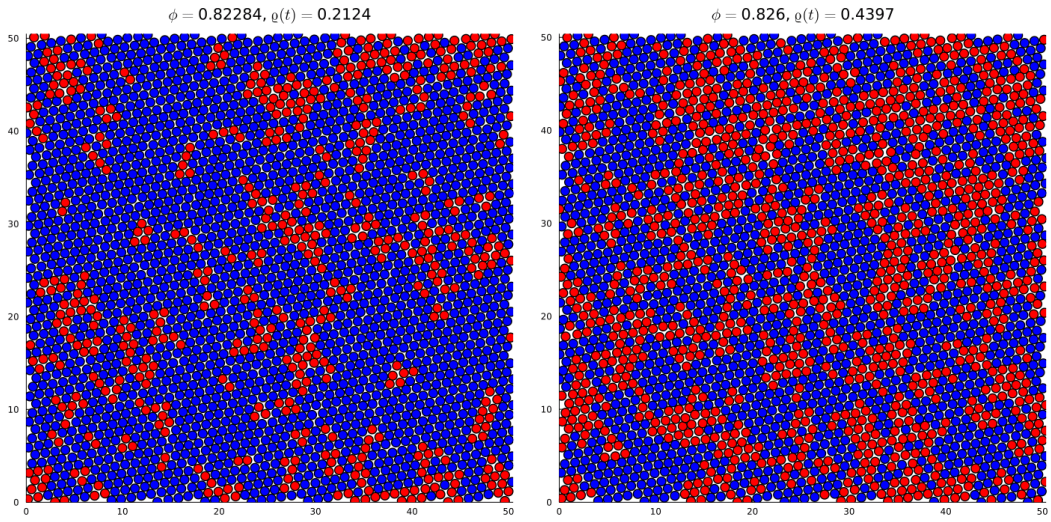

Figure 4.3: Snapshots of the activity for two different packing fractions at steady state in the active phase. Active particles are labelled red, while passive particles are blue.

Figure 4.4 shows the relaxation of the fraction of active particles from an ordered configuration at different packing fractions. The average $\langle\cdot\rangle$ is performed over 24 realisations of the process for a system of approximately 42500 particles. Below

the critical packing fraction ϕ_c, the dynamics reach an absorbing state where the order parameter vanishes, while above ϕ_c, the activity fluctuates around a non-zero value.

To characterise the transition we measure several quantities near the critical point, in order to estimate its critical exponents.

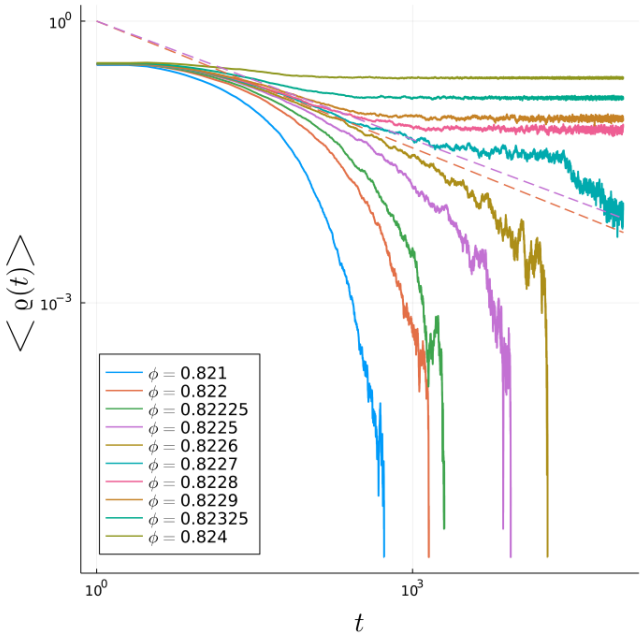

Figure 4.4: Time dependence of the order parameter starting from an ordered configuration. For the first five densities (absorbing phase), $\langle\rho\rangle$ decays to zero. For last five densities (active phase), $\langle\rho\rangle$ fluctuates around its average value. The two dashed lines represent the scaling laws $\langle\rho(t)\rangle \sim t^{-\alpha}$ for DP (orange) and CPD (purple) at criticality.

4.3.1 Finite-size effects

As already mentioned in section 2.1.2, fluctuations of the order parameter in the active phase are due to the finite size of the system in a computer simulation. In absorbing phase transitions, finite-size effects are particularly relevant, since fluctuations may bring the system into an absorbing state even if an infinite

system would have stayed active forever. For this reason, characterising absorbing transitions in experiments and computer simulations is a difficult task, since one has to consider larger and larger systems to get meaningful results near the critical point.

In this project we consider four system sizes ($L = 50$, 100, 200, 300, where the diameter σ of the particles is the unit length) with approximately 2650, 10600, 42500 and 95700 particles. For each system size and for some values of the packing fraction near the critical point we run n_{sim} independent simulations (usually $n_{\text{sim}} = 24$) and we keep only the packing fractions where all simulations for that system size reached the same phase (active or absorbing) in the steady state.

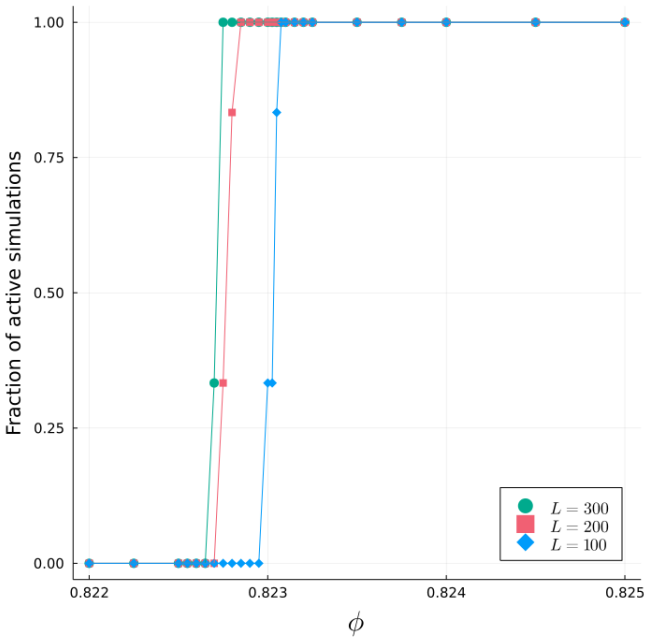

Figure 4.5: Fraction of active simulations for different system sizes. The estimate critical packing fraction decreases when the system size increases.

4.3.2 Order parameter

To quantify the decay of the order parameter at steady state approaching the critical point from above, we measure $\langle \varrho(\infty) \rangle$ as follows: for each independent simulation we consider M measurements of ϱ at steady state from t_{steady} to $t_{\max}$, where t_{steady} is defined as the first instant where the value of $\varrho(t)$ gets 'close' to its last measured value (with a tolerance of 0.005) and $t_{\max}$ is the number of iterations of the algorithm. Then, we average ϱ over $M\, n_{\text{sim}}$ samples. The y-errorbar in $\langle \varrho(\infty) \rangle$ is taken as the empirical standard deviation over these samples divided by $\sqrt{n_{\text{sim}} - 1}$ (figure 4.6).

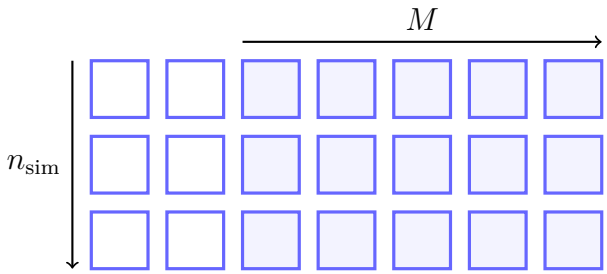

Figure 4.6: Schematic representation of the averaging procedure.

Moving to larger systems allows to investigate packing fractions closer to the critical point (figure 4.7). We fit the results for the largest system with the two power laws for DP and CDP

$$\langle \varrho(\infty) \rangle \sim a^{\text{DP}} \left(\phi - \phi_c^{\text{DP}} \right)^{0.58}, \qquad \phi > \phi_c^{\text{DP}} \tag{4.2a}$$

$$\langle \varrho(\infty) \rangle \sim a^{\text{CDP}} \left(\phi - \phi_c^{\text{CDP}} \right)^{0.64}, \qquad \phi > \phi_c^{\text{CDP}}, \tag{4.2b}$$

where a^{DP}, a^{CDP}, ϕ_c^{DP} and ϕ_c^{CDP} are free parameters.

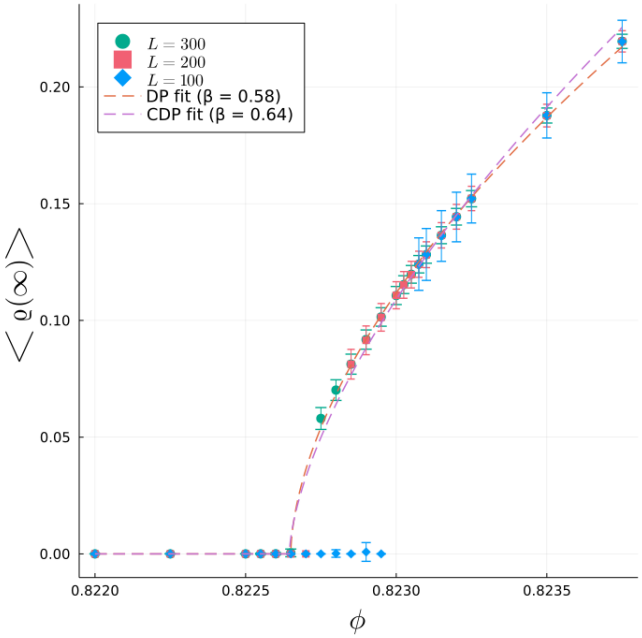

Figure 4.7: Critical scaling of the order parameter at steady state for different system sizes. Because of finite size effects, the critical packing fraction seems to be shifted towards higher values for smaller systems.

4.3.3 Fluctuations at steady state

Fluctuations of the order parameter at steady state (2.14) are relatively easy to measure and can be used to estimate the critical exponent γ'. To practically measure χ we take the variance over the same samples considered for $\langle \varrho(\infty) \rangle$.

We fit the data with the power law

$$\chi \sim b^{\mathrm{TB}} (\phi - \phi_c)^{-0.49}, \qquad \phi > \phi_c, \tag{4.3}$$

where b^{TB} and ϕ_c are free parameters and 0.49 is the value of γ' measured in TB with the same procedure (figure 4.8). The value of γ' is different from that of DP and CDP since fluctuations are measured in the canonical ensemble, where the number of particles is not allowed to fluctuate. In the original work [19], the authors measured χ in the grand-canonical ensemble through the partial structure

factor and reported an exponent close to to that of DP (see table 2.3).

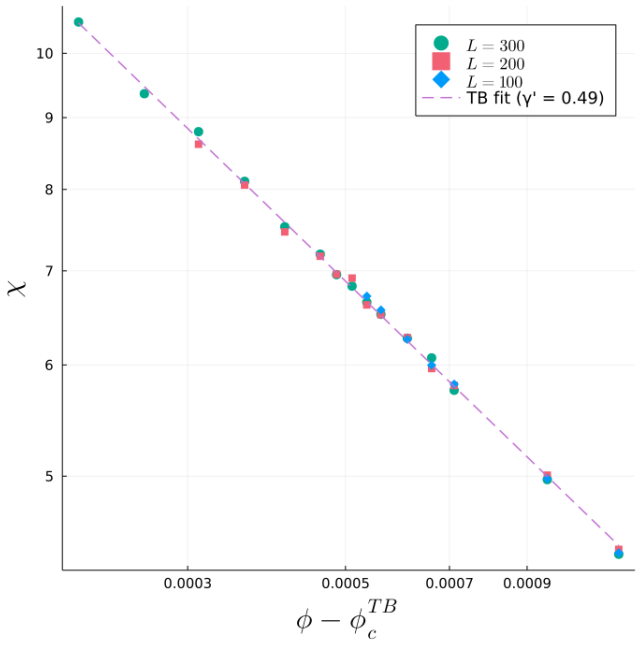

Figure 4.8: Critical scaling of the fluctuations at steady state.

4.3.4 Timescales

In order to determine the exponent $\nu_\parallel$ we measure two different timescales independently. We define the relaxation time τ_r as the number of steps needed to reach an absorbing state in the absorbing phase ($\phi < \phi_c$) or as the first time step where the value of $\langle \varrho(t) \rangle$ gets 'close' to $\langle \varrho(\infty) \rangle$ (tolerance set to 0.005) in the active phase ($\phi > \phi_c$). We fit the results with the power laws

$$\tau_r \sim \begin{cases} c_-^{\mathrm{DP}} \left| \phi - \phi_c^{\mathrm{DP}} \right|^{-1.3}, & \phi < \phi_c \\ c_+^{\mathrm{DP}} \left| \phi - \phi_c^{\mathrm{DP}} \right|^{-1.3}, & \phi > \phi_c \end{cases} \tag{4.4a}$$

$$\tau_r \sim \begin{cases} c_-^{\mathrm{CDP}} \left| \phi - \phi_c^{\mathrm{CDP}} \right|^{-1.23}, & \phi < \phi_c \\ c_+^{\mathrm{CDP}} \left| \phi - \phi_c^{\mathrm{CDP}} \right|^{-1.23}, & \phi > \phi_c, \end{cases} \tag{4.4b}$$

where c_-^{DP}, c_+^{DP}, c_-^{CDP}, c_+^{CDP}, ϕ_c^{DP} and ϕ_c^{DP} are free parameters (figure 4.9).

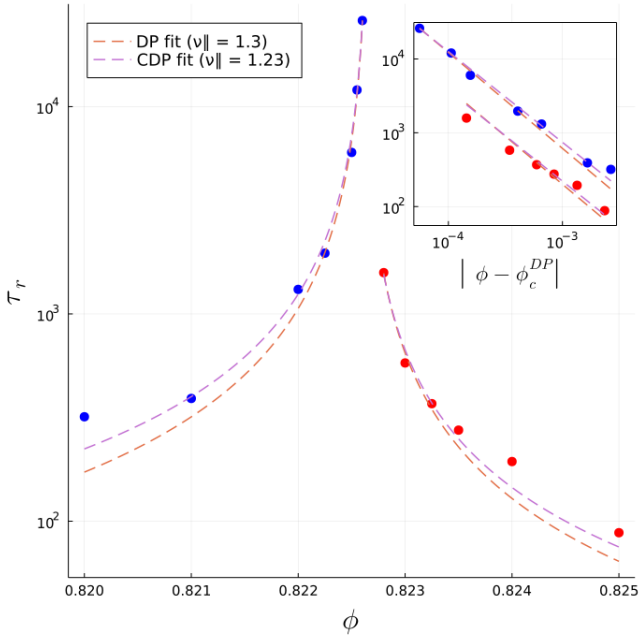

Figure 4.9: Critical scaling of the relaxation time in the two phases.

To measure the autocorrelation function

$$C(\Delta t) = \frac{\langle \varrho(t+\Delta t)\varrho(t)\rangle - \langle \varrho\rangle^2}{\langle \varrho^2\rangle - \langle \varrho\rangle^2} \tag{4.5}$$

we average over $(M - \Delta t)n_{\text{sim}}$ samples at steady state for each Δt. At $\Delta t = 0$, the autocorrelation is equal to 1, while it decays to zero in the limit $\Delta t \to +\infty$ (figure 4.10, left panel).

We define the correlation time τ_c in the active phase by setting $C(\tau_c) = 1/e$. To fit the results we use the power laws

$$\tau_c \sim d^{\text{DP}}\left(\phi - \phi_c^{\text{DP}}\right)^{-1.3}, \qquad \phi > \phi_c^{\text{DP}} \tag{4.6a}$$

$$\tau_c \sim d^{\text{CDP}}\left(\phi - \phi_c^{\text{CDP}}\right)^{-1.23}, \qquad \phi > \phi_c^{\text{CDP}}, \tag{4.6b}$$

with the four free parameters d^{DP}, d^{CDP}, ϕ_c^{DP} and ϕ_c^{CDP}. As we expect, both timescasles diverge at the critical point.

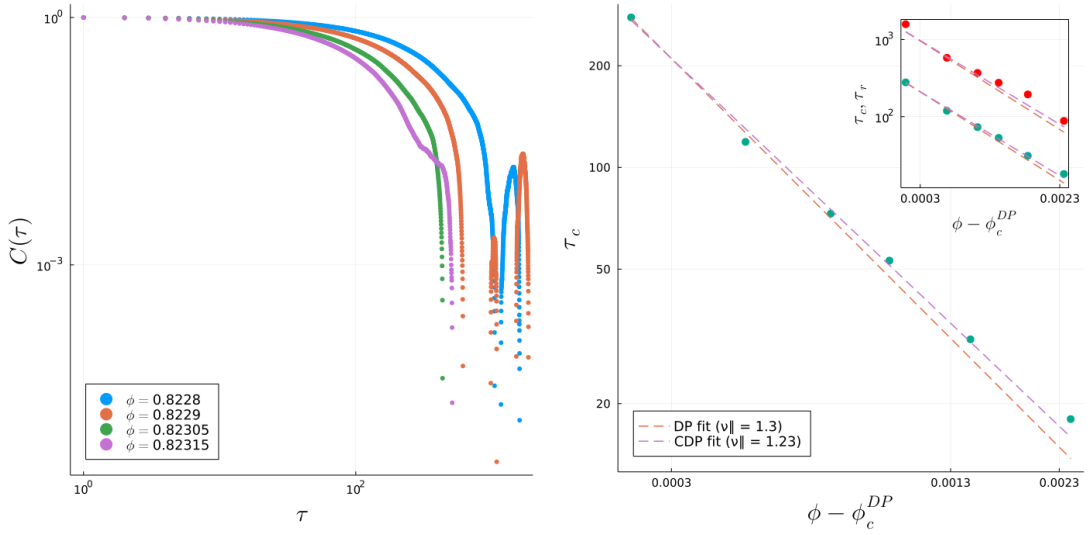

Figure 4.10: Left panel: autocorrelation function for different packing fractions. Right panel: critical scaling of the correlation time. Inset: comparison between the two timescales in the active phase.

4.3.5 Critical packing fraction

To estimate the critical packing fraction we consider the values of ϕ_c^{DP} and ϕ_c^{CDP} obtained for the different interpolations (table 4.1). The average value is $\phi_c = 0.8226$ for both DP and CDP.

	ϕ_c^{DP}	ϕ_c^{CDP}
ϱ	0.82265	0.82264
τ_r	0.82259	0.82259
τ_c	0.82256	0.82256

Table 4.1: Critical packing fractions from different interpolations.

4.4 Discussion

Our findings of both diverging lengthscales and timescales confirm the existence of a dynamical phase transition in our model. As in the original work by Tjhung and Berthier, the universality class of our model is compatible with both DP and CDP. Since the two sets of exponents are very close to one another, distinguishing between these two classes is a difficult task and would require a large numerical effort [19]. Given the nature of both our model and TB, where the number of absorbing states is infinite and the number of particles is conserved, it is reasonable to expect that both models belong to the CDP universality class.

In any case, the two set of exponents are both very different from the one measured by Gosh *et al.* [49]. This suggests that the ordering due to crystallisation is irrelevant to the absorbing phase transition and confirms the robustness of the CDP class [1, 21]. Yet, the interplay between the two dynamical transitions is a rich and interesting phenomenon, which we will present in detail in the next chapter.

Chapter 5

Coupling with the ordering transition

Unlike previous works [19, 20, 21], our model generates ordered steady state configurations, in which particles fluctuate around the sites of a perfect hexagonal lattice. In this chapter we analyse the ordering transition from a random initial configuration by measuring the relevant physical quantities across the absorbing transition. We will also discuss the stability of the crystalline state and we will show that it behaves very differently from an equilibrium harmonic solid at finite temperature.

5.1 Quantifying order

To monitor the ordering transition we measure some of the quantities we presented in section 3.3 for different packing fractions and system sizes.

For each independent simulation and for each of the M samples stored from t_0 to $t_{\max}$ we determine the Voronoi tessellation through the package `VoronoiCells`

[54]. We use the set of neighbours to evaluate

$$\psi_6(\boldsymbol{r}_i, t) = \frac{1}{|\partial i|} \sum_{j \in \partial i} \mathrm{e}^{6\mathrm{i}\theta_{ij}}, \tag{5.1}$$

for each particle. In the following snapshots of the system, the phase of ψ_6 is mapped to colors according to the color scheme in figure 5.1.

Figure 5.1: Cyclic color scheme for the phase of ψ_6.

For each configuration we evaluate

$$\Psi_6(t) = \frac{1}{N} \left| \sum_{i=1}^{N} \psi_6(\boldsymbol{r}_i, t) \right| \tag{5.2a}$$

$$\Psi_{|6|}(t) = \frac{1}{N} \sum_{i=1}^{N} |\psi_6(\boldsymbol{r}_i, t)|. \tag{5.2b}$$

The first quantity is the bond-orientational order parameter (3.28). It measures the global orientational order of the system, which is closer to one the more perfect the crystal. In contrast, $\Psi_{|6|}$ does not account for different orientations in the sample and is close to one even in a polycrystal.

The mean value $\langle \Psi_6(\infty) \rangle$ is taken over M measurements of Ψ_6 from t_{steady} to $t_{\max}$ (see figure 4.6) for n_{sim} independent simulations. The y-errorbar in $\langle \Psi_6(\infty) \rangle$ is taken as the empirical standard deviation over these samples divided by $\sqrt{n_{\text{sim}} - 1}$.

We define the fluctuations of Ψ_6 as

$$\chi_6 = N\Big(\big\langle \Psi_6(\infty)^2 \big\rangle - \langle \Psi_6(\infty) \rangle^2 \Big). \tag{5.3}$$

To practically measure χ_6 we take the variance over the same samples considered for $\langle \Psi_6(\infty) \rangle$.

For each of the n_{sim} configurations at $t_{\max}$ we exploit the Voronoi tessellation to measure the bulk fraction ρ_D of misaligned particles, which can be used to

estimate the fraction of topological defects. The mean values $\left\langle \Psi_{|6|}(\infty) \right\rangle$ and $\langle \rho_D(\infty) \rangle$ are simply the empirical averages of $\Psi_{|6|}$ and ρ_D evaluated at $t_{\max}$ over n_{sim} samples. The y-errorbars are taken from the empirical standard deviation divided by $\sqrt{n_{\text{sim}} - 1}$.

We measure the pair correlation function (3.23) as follow: for each stored configuration at steady state we loop over pairs of particles and we build an histogram h_D of the relative distances with bins of length δr (usually $\delta r = 0.02$). Then, we normalise h_D as

$$g(r) = \frac{2L^2}{\pi N^2 \Big((r + \delta r)^2 - r^2 \Big)} \, h_D(r), \tag{5.4}$$

with $r = 0,\, \delta r,\, 2\delta r,\, \ldots,\, r_{\max}$. Finally, we average over the $M\, n_{\text{sim}}$ stored configurations.

Similarly, we measure the bond orientational correlation function (3.29) as follow: for each stored configuration at steady state we loop over pairs of particles and we build an histogram h_{D6} of the product $\psi_6(\boldsymbol{r}_i)\psi_6^\star(\boldsymbol{r}_j)$ with bins of length δr. Then, we normalise as

$$g_6(r) = \frac{2L^2}{\pi N^2 \Big((r + \delta r)^2 - r^2 \Big)} \, \mathrm{Re}\left(h_{D6}(r) \right) \tag{5.5}$$

and we average over the stored configurations.

To measure the structure factor (3.25) for each configuration we generate a lattice of $(n_{\max} + 1)(2n_{\max} + 1)$ points

$$q_x = \frac{2\pi}{L} \, n_x, \quad -n_{\max} \leq n_x \leq n_{\max} \tag{5.6a}$$

$$q_y = \frac{2\pi}{L} \, n_y, \quad 0 \leq n_y \leq, n_{\max} \tag{5.6b}$$

with $n_x, n_y \in \mathbb{Z}$. For each point $\boldsymbol{q} \neq (0{,}0)$ we compute

$$S_{2D}(\boldsymbol{q}) = \frac{1}{N} \left(\left(\sum_{i=1}^{N} \cos\left(\boldsymbol{q} \cdot \boldsymbol{r}_i \right) \right)^2 + \left(\sum_{i=1}^{N} \sin\left(\boldsymbol{q} \cdot \boldsymbol{r}_i \right) \right)^2 \right).$$

Then, we average all points such that

$$q \leq \|\boldsymbol{q}\| \leq q + \delta q \tag{5.7}$$

and, finally, we average over the $M\, n_{\mathrm{sim}}$ stored configurations.

5.2 Relaxation towards steady state

Starting from a random initial configuration, the approach to the crystalline state resembles the relaxation of coarsening systems. Figure 5.2 shows three snapshots taken from supplementary movie 3 at different times. The system initially organises into multiple crystalline regions with different orientation, while, at large times, the dynamics are driven by the motion of grain boundaries and by the mutual annihilation of localised topological defect with opposite charges. The true steady state of an infinite system is thus expected to be a perfect crystal in the active phase, since defects are not spontaneously generated by the dynamics for our choice of parameters ($\epsilon = 0.1$). Note that, for larger values of ϵ, defects appear and vanish spontaneously at steady state, leading to less ordered configurations.

5.2.1 Defect analysis

Snapshots of the system at different times show different types of defects (figure 5.3). Vacancies are fixed in place and can be removed by motile defects. Note that vacancies have zero topological charge. Dislocations can instead move freely along the direction of their Burgers vector. Two dislocations with different charges can interact: if they lie on the same glide line they mutually annihilate, otherwise they may merge into a single dislocation that conserves the topological charge (see supplementary movie 3). Different types of more complex clusters can form and interact with other defects. At higher packing fractions, unphysical defects appear

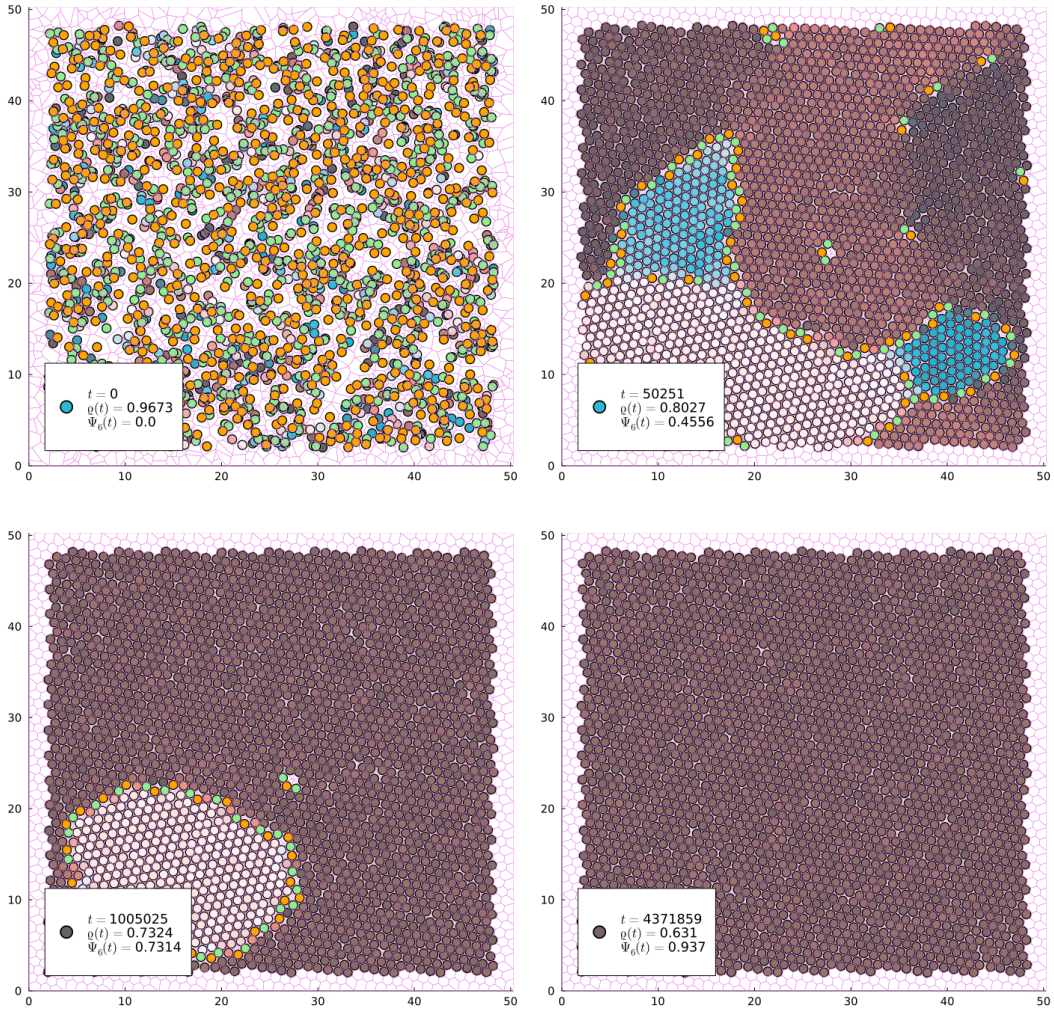

Figure 5.2: Snapshots of the system at different times for $\phi = 0.83$. The phase of ψ_6 is mapped to colors using the scheme in figure 5.1. Particles with less (more) than six neighbours are coloured green (orange).

made of particles stacked on top of each other. Finally, regions with different orientation are delimited by extended grain boundaries.

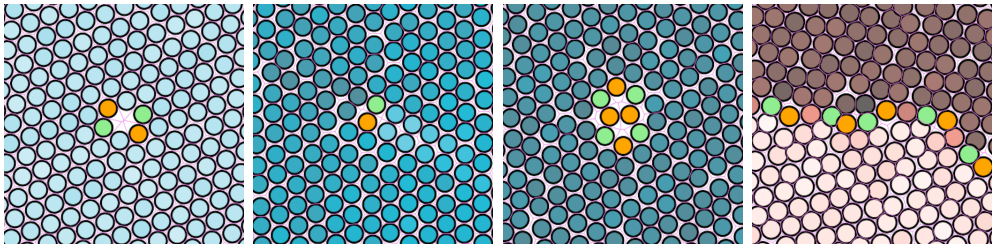

Figure 5.3: Map of the defects in the system. From left to right: vacancy, dislocation, cluster, grain boundary.

5.2.2 Finite-size effects

One of the greatest challenges we faced in this project has been the slowdown in the relaxation towards steady state due to finite-size effects. In some simulations, grain boundaries extend throughout the whole system, resulting in very stable configurations that do not reach the steady state during the simulation time (figure 5.4). We can safely say that these configurations are an artifact of periodic boundary conditions, since the typical size of the domains with the same orientation at a given packing fraction grows with the system size L. This is very different from the behaviour of the typical lengthscale of domains in the absorbing phase, as we will discuss in the following sections. To limit this effect, we manually remove such configurations from the samples we consider to measure relevant quantities.

5.3 Order across the transition

Figures 5.5 show the behaviour of $\langle \Psi_6(\infty) \rangle$, $\left\langle \Psi_{|6|}(\infty) \right\rangle$ and $\langle \rho_D(\infty) \rangle$ for several packing fractions and for two different system sizes near the critical point. All three quantities exhibit a singularity at $\phi = \phi_c$, confirming that the absorbing and ordering transitions take place at the same critical packing fraction. In the active phase, we report data from only one system size, since the coarsening time of larger systems exceeds our observation time.

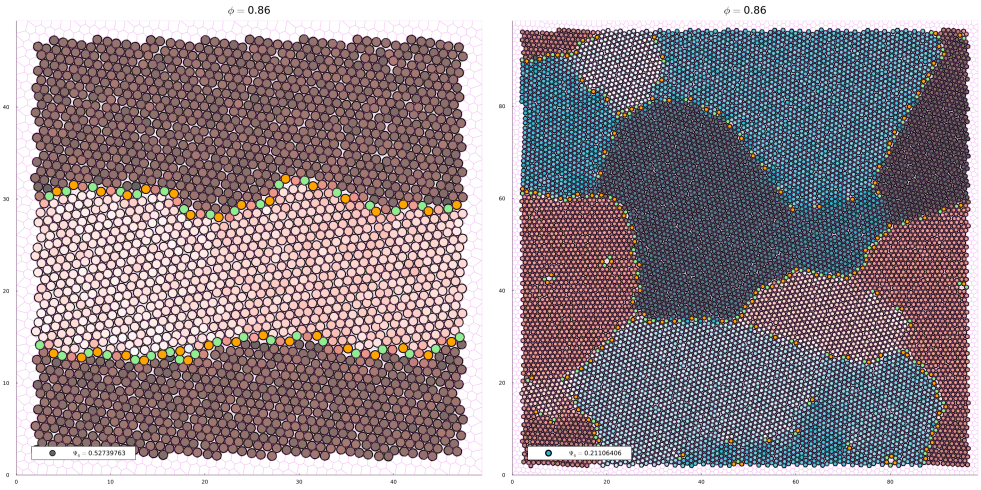

Figure 5.4: Stable configurations due to finite size effects for $L = 50$, 100.

5.3.1 Absorbing phase

When $\phi \ll \phi_c$, the system quickly reaches a disordered absorbing state, since it has no time to organise. In contrast, when $\phi \to \phi_c^-$, particles organise in multiple domains with different orientation during the relaxation process, but at some point the system stops moving before reaching full orientational order. When observing different absorbing configuration at increasing $\phi \lesssim \phi_c$, the typical size $R(\phi)$ of the crystalline domains increases and it is expected to diverge at the critical point. Contrary to the typical size of the domains due to finite-size effects, $R(\phi)$ is independent of L (figure 5.6).

The behaviour of the two correlation functions $g(r)$ and $g_6(r)$ (figure 5.7) shows that the lengthscales characterising the orientational and translational order in the absorbing phase are the same. The growing lengthscale $R(\phi)$ can thus be extracted from the decay of one of the two correlation functions.

In the absorbing phase, $\langle \Psi_6(\infty) \rangle$ is quite small, since contributions to the phase of Ψ_6 from different polycristalline regions tend to cancel out. For this reason, we expect $\langle \Psi_6(\infty) \rangle = 0$ for an infinite system in the absorbing phase.

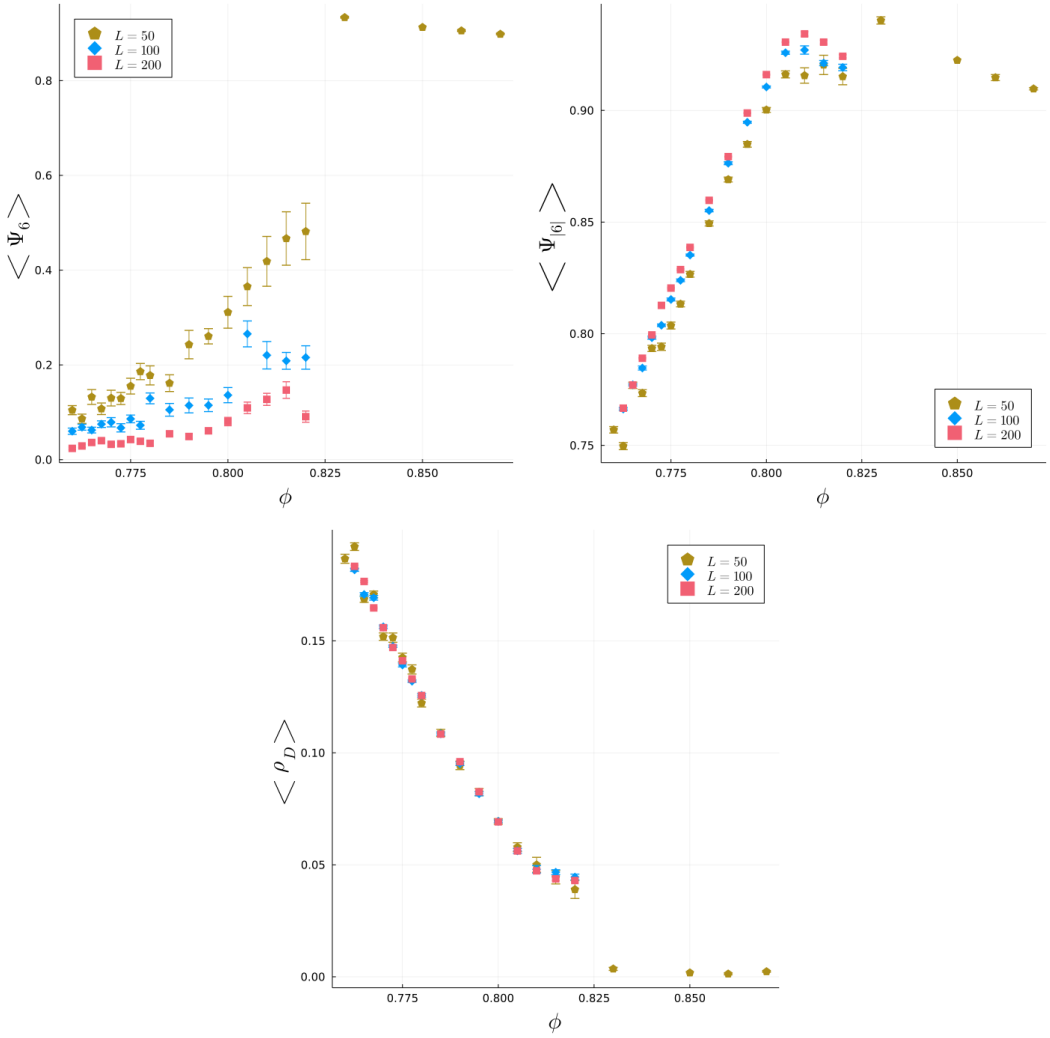

Figure 5.5: Critical behaviour of $\langle \Psi_6(\infty) \rangle$, $\left\langle \Psi_{|6|}(\infty) \right\rangle$ and $\langle \rho_D(\infty) \rangle$ starting from random initial configurations.

On the other hand, $\left\langle \Psi_{|6|}(\infty) \right\rangle$ grows continuously from $\left\langle \Psi_{|6|}(\infty) \right\rangle \approx 0$, when $\phi \ll \phi_c$ and it approaches one when polycrystals start to emerge.

The fraction $\langle \rho_D(\infty) \rangle$ of misaligned particles decreases monotonically as $\phi \to \phi_c^-$, as more and more defects have time to annihilate.

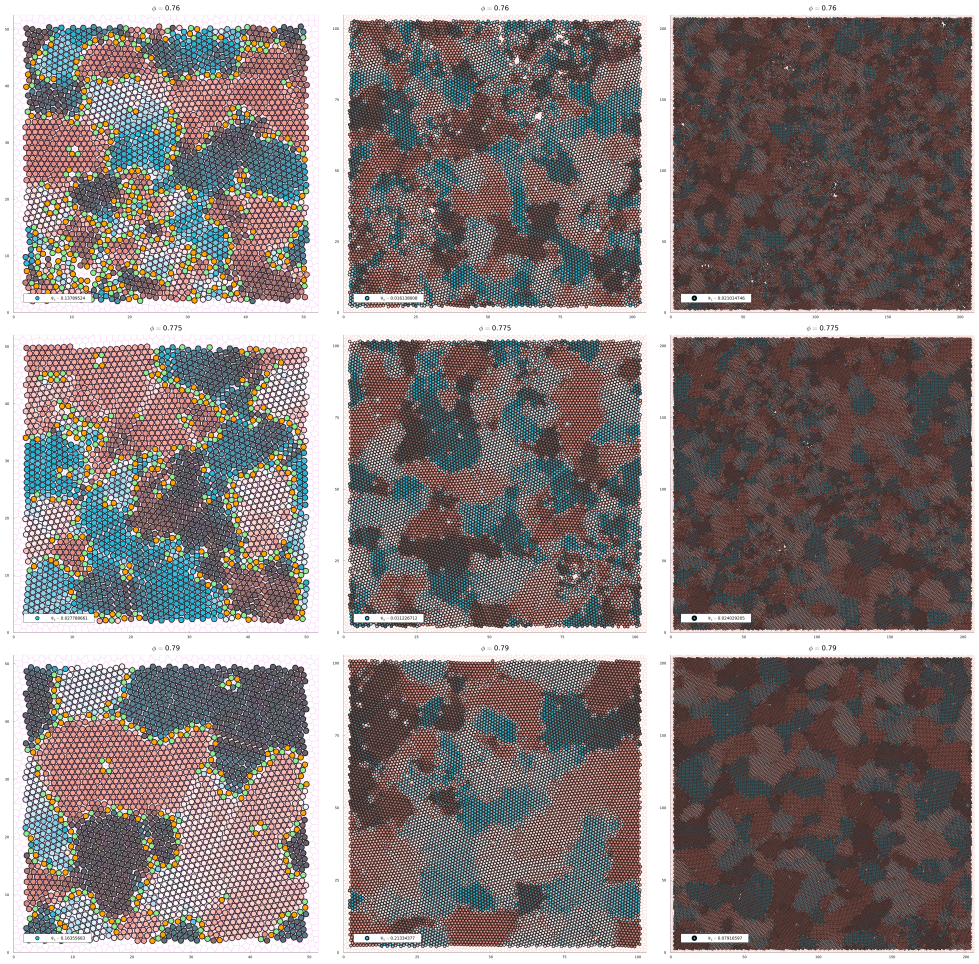

Figure 5.6: Snapshots of several absorbing states at different packing fractions for $L = 50$, 100, 200. The typical size $R(\phi)$ of the crystalline domains grows with ϕ and is independent of L.

5.3.2 Active phase

As we already discussed, the active steady state of an infinite system is expected to be a perfect crystal with no defects for our choice of parameters. In a finite-size system, some defects may survive in the steady state (e.g. isolated dislocation that cannot disappear without interacting with another defect). These defects frustrate the crystal by locally increasing the packing fraction and, consequently, the activity. However, spatial fluctuations of activity are distributed throughout the system and

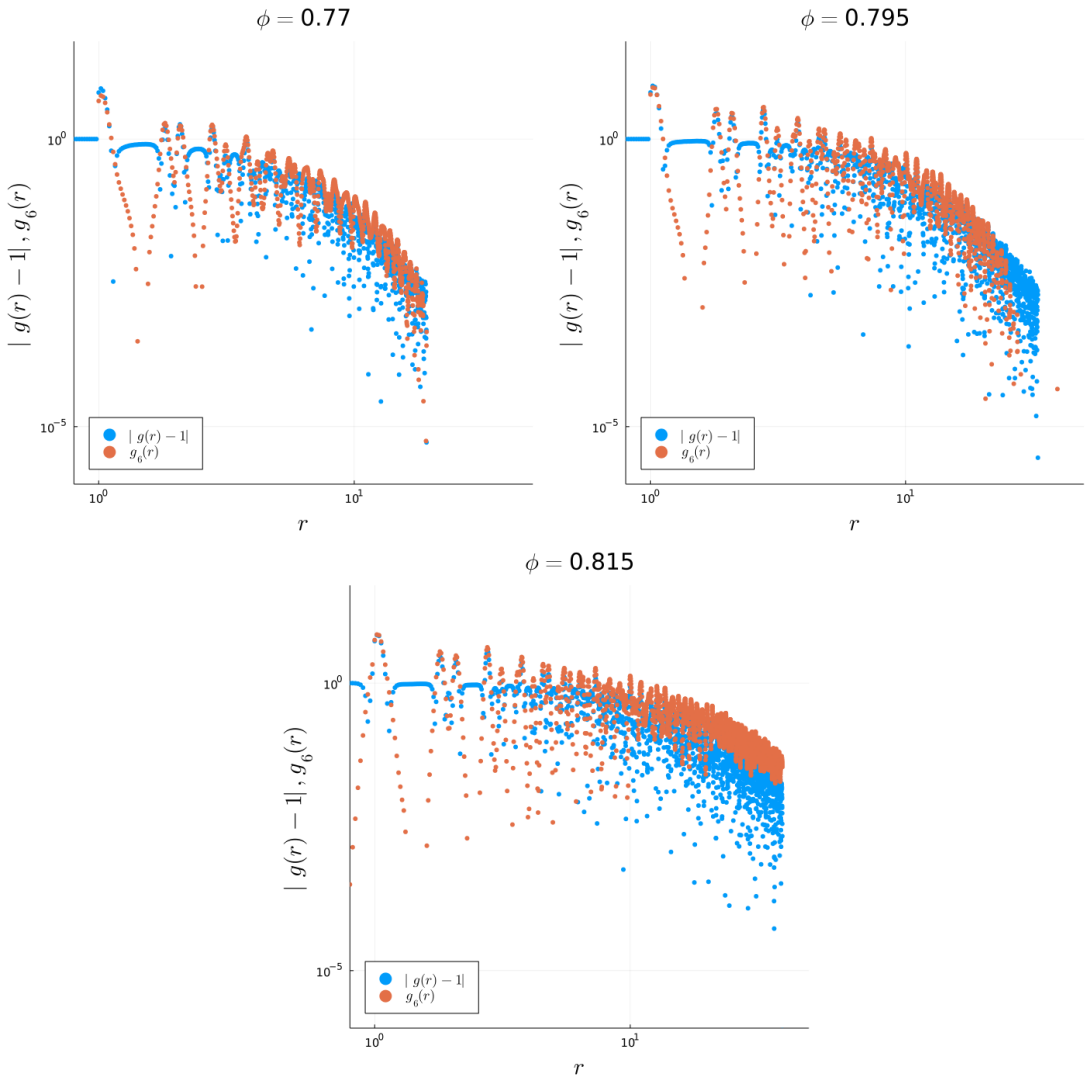

Figure 5.7: Comparison between $g(r)$ and $g_6(r)$ at different packing fractions in the absorbing phase. The typical length $R(\phi)$ can be extracted from the decay of the two correlation functions.

do not interact with the defect itself.

The bond orientational order parameter $\langle \Psi_6(\infty) \rangle$ reaches a maximum at the critical point and it decreases slowly as the the packing fraction increases in the active phase. The activity has thus the effect of perturbing the crystal, reducing the global order.

The behaviour of $\left\langle \Psi_{|6|}(\infty) \right\rangle$ is qualitatively the same as $\langle \Psi_6(\infty) \rangle$, since the system is characterised by a single crystalline region with the same orientation.

In the active phase, both correlation functions $g(r)$ and $g_6(r)$ show discrete peaks occurring at the sites of the hexagonal lattice (figure 5.8, inset). This indicates that the system reaches both orientational and translational order in the active phase. The pair correlation has sharp peaks up to the maximal distance we probed for the largest system ($L = 300$), which is a signal of long-range order.

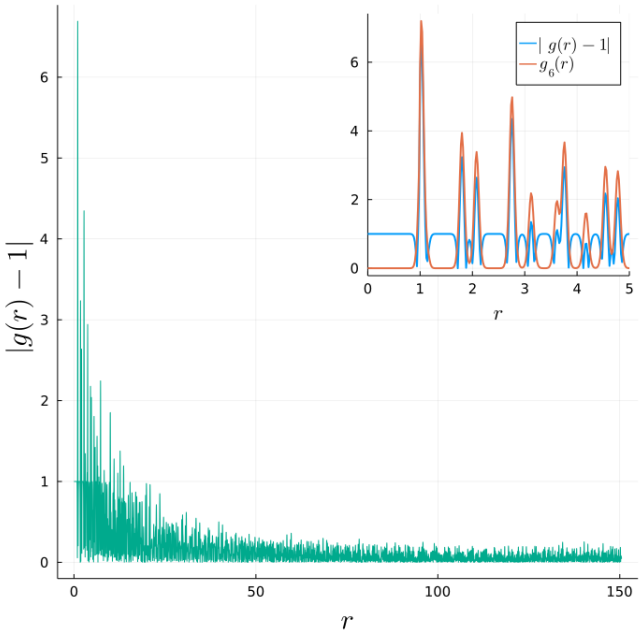

Figure 5.8: Pair correlation function for $L = 300$ in the active phase ($\phi = 0.83$). Inset: peaks of $g(r)$ and $g_6(r)$ corresponding to the sites of the hexagonal lattice.

5.4 Building a two-dimensional crystal

In section 3.2 we argued that a two-dimensional crystal cannot exist at equilibrium, since long-range correlations of the displacement field (i.e. phonons) destroy the long-range translational order. Out of equilibrium, equipartition no longer holds, so

in principle it should be possible to create a dynamical rule distinct from thermal fluctuations that allows long-range crystalline order in two dimensions.

To decide whether our model can generate two-dimensional crystals, we consider the mean-squared displacement (MSD) in the active phase for different system sizes. We showed in (3.14) that the behaviour of the MSD is related to the displacement structure factor of the

$$S_{\hat{u}}(\boldsymbol{q}) = \left\langle |\hat{\boldsymbol{u}}(\boldsymbol{q})|^2 \right\rangle . \tag{5.8}$$

Specifically, if the structure factor converges as $q \to 0$ (or if it diverges as $S_{\hat{u}} \sim q^{-n}$, with $n < 2$), then the MSD in the long time limit converges with the system size L. This means that particles cannot move far away from their equilibrium positions and that the crystal is stable.

We measure the displacement of each particle as

$$\boldsymbol{u}_i(t) = \boldsymbol{r}_i(t) - \boldsymbol{r}_i^0, \tag{5.9}$$

where $\boldsymbol{r}_i^0$ denotes the average position of particle i at steady state. Then, the displacement structure factor is simply

$$S_{\hat{u}}(\boldsymbol{q}) = \frac{1}{N} \left\langle \left(\sum_{i=1}^{N} \boldsymbol{u}_i(\infty) \cos\left(\boldsymbol{q} \cdot \boldsymbol{r}_i^0\right) \right)^2 + \left(\sum_{i=1}^{N} \boldsymbol{u}_i(\infty) \sin\left(\boldsymbol{q} \cdot \boldsymbol{r}_i^0\right) \right)^2 \right\rangle \tag{5.10}$$

at steady state, where the ensemble average is taken over many simulations with different initial conditions (starting from the "perfect" crystal).

Figure 5.9 shows that the displacement structure factor converges at low q. This is fundamentally related to the conservation of the center of mass in the dynamical rule that defines our model, which constraints the total displacement to be conserved. The value of q at which $S_{\hat{u}}$ reaches the plateau can be used to identify a growing lengthscale in the system as $\phi \to \phi_c^+$.

The mean-squared displacement is measured as

$$\mathrm{MSD}(t) = \frac{1}{N} \left\langle \sum_{i=1}^{N} \|\boldsymbol{r}_i(t) - \boldsymbol{r}_i(0)\|^2 \right\rangle . \tag{5.11}$$

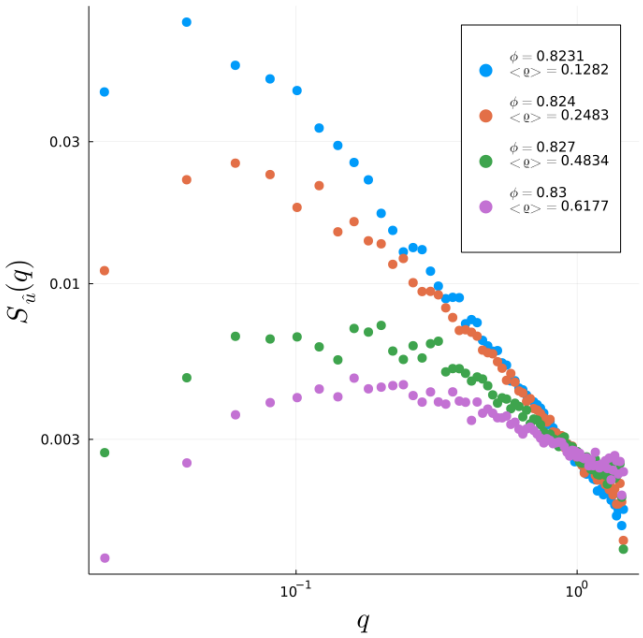

Figure 5.9: Displacement structure factor for several packing fractions measured for $L = 300$. The legend reports the average activity for each value of ϕ.

Figure 5.10 (left panel) shows the MSD at different packing fractions. As $\phi \to \phi_c^+$, the timescale needed to reach the plateau increases, in agreement with the expected critical slowing down near the critical point. The value of the plateau increases slightly with ϕ, since multiple overlaps become more common at larger packing fractions.

Figure 5.10 (right panel) confirms that the plateau of the MSD does not depend on L and that the crystal is thus stable.

5.5 Discussion

Our results show that the two dynamical phase transitions occur at the same time and are deeply coupled. Random organisation at high densities can thus be seen as a non-equilibrium crystallisation process in the context of absorbing phase transitions.

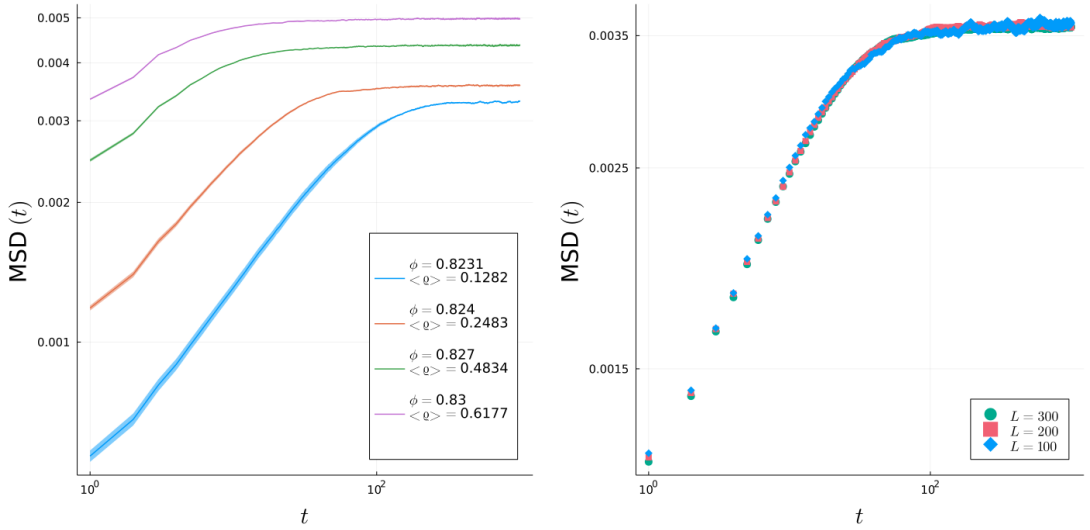

Figure 5.10: Left panel: MSD for $L = 300$ at several packing fractions. The value of the plateau increases slightly with ϕ because of multiple overlaps between particles become more common. Right panel: dependence of the MSD on the system size for $\phi = 0.824$.

A detailed analysis of the mean square displacement and displacement structure factor establishes that our model breaks the equipartition of energy in a way that allows two-dimensional crystals to be stable. This result is particularly interesting, since long-range translational order cannot exist in two dimensions at equilibrium. Despite being driven by the interaction of topological defects, the crystallisation process in our model is very different from the equilibrium liquid-solid transition in two dimensions, which passes through the intermediate hexatic phase.

Conclusion

By tuning the control parameters of a simple numerical model, this work shows that two-dimensional crystallisation can occur at the critical point of an absorbing phase transition.

Random organisation is a rich and developing context, which provides access to the reversible-irreversible transition in periodically driven suspensions through experimental and numerical methods. In this work, such model has been pushed to a region of parameter space where the self-organisation process leads to ordered configurations, which made it possible to study the absorbing transition in the presence of an ordering field.

Our findings show that the coupling with the ordering transition is irrelevant to the absorbing transition, since the set of critical exponents coincides with that of previous models. This represents further evidence of the robustness of the (conserved) directed percolation universality class and disproves some of the results in [49]. Yet, the ordering transition in our model has unique features fundamentally due to the presence of an active and an absorbing phase.

In the last part of this work it is shown that the dynamical rule defining our model can be used as a protocol to generate two-dimensional crystals with long-range translational order. This result can only be achieved out of equilibrium, since Mermin-Wagner theorem forbids crystallisation in two dimensions. In principle, similar outcomes could be found in other non-equilibrium models, such as dense

active matter systems.

The research activity is going to continue beyond this thesis. We are currently studying larger systems in order to get better estimates of the critical exponents and refine our results. This task involves a significant computational effort. We are also developing a one-dimensional version of the model to compare with the two-dimensional case. Large systems in one dimension are easier to analyse and could provide new insights on both dynamical transitions.

Our findings open several opportunities to carry on the research. An exciting option would be the introduction of polydispersity in our model, so that the crystalline order is replaced by dense jammed configurations. In this scenario, machine learning tools could be employed to investigate the coupling between the absorbing phase transition and hyperuniformity.

Bibliography

[1]M. Henkel, H. Hinrichsen, and S. Lübeck, *Non-Equilibrium Phase Transitions, Volume 1: Absorbing Phase Transitions*, 2009th edition (Springer, 2009) (cit. on pp. 1, 9, 11, 13, 15–17, 48).

[2]D. Tong, *Kinetic theory*, University of Cambridge Graduate Course, 2012 (cit. on p. 1).

[3]J. Kurchan, «Six out of equilibrium lectures», `10.48550/ARXIV.0901.1271` (2009) (cit. on pp. 1, 5, 7).

[4]D. Anderson, *Markov Chain lecture notes*, 2008 (cit. on p. 3).

[5]R. Brown, «A brief account of microscopical observations made in the months of june, july, and august, 1827, on the particles contained in the pollen of plants; and on the general existence of active molecules in organic and inorganic bodies», in *The miscellaneous botanical works of robert brown*, Vol. 1, edited by J. J. Bennett, Cambridge Library Collection - Botany and Horticulture (Cambridge University Press, 2015), pp. 463–486 (cit. on p. 4).

[6]L. Dall'Asta, *Lecture Notes on Statistical Field Theory*, 2020 (cit. on pp. 6, 13).

[7]M. Modell and R. Reid, *Thermodynamics and Its Applications*, Prentice-Hall international series in the physical and chemical engineering sciences (Prentice-Hall, 1974) (cit. on p. 8).

[8]R. Livi and P. Politi, *Nonequilibrium Statistical Physics, A Modern Perspective*, 1st edition (Cambridge University Press, 2017) (cit. on pp. 9, 15, 30, 32).

[9]U. Täuber, *Fluctuations and correlations in chemical reaction kinetics and population dynamics*, July 2018 (cit. on p. 9).

[10]H. K. Janssen, «On the nonequilibrium phase transition in reaction-diffusion systems with an absorbing stationary state», Zeitschrift für Physik B Condensed Matter **42**, 151–154 (1981) (cit. on p. 15).

[11]P. Grassberger, «On phase transitions in schlögl's second model», Zeitschrift für Physik B Condensed Matter **47**, 365–374 (1982) (cit. on p. 15).

[12]H. Hinrichsen, «Non-equilibrium critical phenomena and phase transitions into absorbing states», Advances in Physics **49**, 815–958 (2000) (cit. on p. 16).

[13]R. Dickman and R. Vidigal, «Path-integral representation for a stochastic sandpile», Journal of Physics A: Mathematical and General **35**, 7269–7285 (2002) (cit. on p. 16).

[14]J. F. Stilck, R. Dickman, and R. R. Vidigal, «Series expansion for a stochastic sandpile», Journal of Physics A: Mathematical and General **37**, 1145–1157 (2004) (cit. on p. 16).

[15]P. L. Doussal and K. J. Wiese, «Exact mapping of the stochastic field theory for manna sandpiles to interfaces in random media», Physical Review Letters **114**, 10.1103/physrevlett.114.110601 (2015) (cit. on p. 16).

[16]D. J. Pine, J. P. Gollub, J. F. Brady, and A. M. Leshansky, «Chaos and threshold for irreversibility in sheared suspensions», Nature **438**, 997–1000 (2005) (cit. on p. 17).

[17]L. Corté, P. M. Chaikin, J. P. Gollub, and D. J. Pine, «Random organization in periodically driven systems», Nature Physics **4**, 420–424 (2008) (cit. on pp. 17, 18).

[18]L. Corté, S. J. Gerbode, W. Man, and D. J. Pine, «Self-organized criticality in sheared suspensions», Phys. Rev. Lett. **103**, 248301 (2009) (cit. on p. 17).

[19]E. Tjhung and L. Berthier, «Criticality and correlated dynamics at the irreversibility transition in periodically driven colloidal suspensions», Journal of Statistical Mechanics: Theory and Experiment **2016**, 033501 (2016) (cit. on pp. 18–21, 38, 40, 44, 48, 49).

[20]S. Wilken, R. E. Guerra, D. Levine, and P. M. Chaikin, «Random close packing as a dynamical phase transition», Phys. Rev. Lett. **127**, 038002 (2021) (cit. on pp. 18, 19, 36, 49).

[21]C. Ness and M. E. Cates, «Absorbing-state transitions in granular materials close to jamming», Phys. Rev. Lett. **124**, 088004 (2020) (cit. on pp. 18, 19, 48, 49).

[22]S. Torquato and F. H. Stillinger, «Local density fluctuations, hyperuniformity, and order metrics», Phys. Rev. E **68**, 041113 (2003) (cit. on p. 19).

[23]J. Sólyom, *Fundamentals of the Physics of Solids, Volume 1: Structure and Dynamics*, 1st edition (Springer, 2009) (cit. on p. 22).

[24]A. Montorsi, *Notes on Quantum Theory of Condensed Matter*, 2020 (cit. on p. 22).

[25]J. U. Klamser, «Low-dimensional phase transitions in and outside equilibrium», Theses (Sorbonne Université, Dec. 2018) (cit. on pp. 23, 24).

[26]L. F. Cugliandolo and G. Gonnella, *Phases of active matter in two dimensions*, 2018 (cit. on pp. 23, 28, 35).

[27]N. W. Ashcroft and N. D. Mermin, *Solid State Physics* (Holt-Saunders, 1976) (cit. on p. 23).

[28]N. D. Mermin, «Crystalline order in two dimensions», Phys. Rev. **176**, 250–254 (1968) (cit. on p. 26).

[29]J. M. Kosterlitz, «Kosterlitz-Thouless physics: a review of key issues», Reports on Progress in Physics **79**, 026001 (2016) (cit. on p. 26).

[30]V. N. Ryzhov, E. E. Tareyeva, Y. D. Fomin, and E. N. Tsiok, «Berezinskii-Kosterlitz-Thouless transition and two-dimensional melting», Phys. Usp. **60**, 857–885 (2017) (cit. on p. 26).

[31]J. P. Hansen and I. McDonald, *Theory of Simple Liquids* (Academic, London, 1990) (cit. on p. 27).

[32]Y. Komatsu and H. Tanaka, «Roles of energy dissipation in a liquid-solid transition of out-of-equilibrium systems», Phys. Rev. X **5**, 031025 (2015) (cit. on pp. 27, 28, 35, 36).

[33]G. Briand, «Etude expérimentale des phases denses d'un liquide de disques durs actifs», Theses (Université Paris sciences et lettres, Dec. 2017) (cit. on p. 27).

[34]L. Berthier and J. Kurchan, *Lectures on non-equilibrium active systems*, 2019 (cit. on pp. 28, 36).

[35]E. Rožić, *Topological Defects in Physics*, 2019 (cit. on p. 29).

[36]W. T. M. Irvine, A. D. Hollingsworth, D. G. Grier, and P. M. Chaikin, «Dislocation reactions, grain boundaries, and irreversibility in two-dimensional lattices using topological tweezers», Proceedings of the National Academy of Sciences **110**, 15544–15548 (2013) (cit. on p. 29).

[37]A. Bray, «Theory of phase-ordering kinetics», Advances in Physics **43**, 357–459 (1994) (cit. on p. 30).

[38]P. Digregorio, D. Levis, L. F. Cugliandolo, G. Gonnella, and I. Pagonabarraga, *Unified analysis of topological defects in 2d systems of active and passive disks*, 2021 (cit. on p. 30).

[39]E. Bernard, «Algorithms and applications of the monte carlo method : two-dimensional melting and perfect sampling», (2011) (cit. on p. 31).

[40]L. Dall'Asta, *Kinetics of Phase Transitions*, 2020 (cit. on p. 33).

[41]A. J. Bray and A. D. Rutenberg, «Growth laws for phase ordering», Phys. Rev. E **49**, R27–R30 (1994) (cit. on p. 34).

[42]M. Engel, J. A. Anderson, S. C. Glotzer, M. Isobe, E. P. Bernard, and W. Krauth, «Hard-disk equation of state: first-order liquid-hexatic transition in two dimensions with three simulation methods», Phys. Rev. E **87**, 042134 (2013) (cit. on p. 35).

[43]U. Gasser, «Crystallization in three- and two-dimensional colloidal suspensions», Journal of Physics: Condensed Matter **21**, 203101 (2009) (cit. on p. 35).

[44]K. Strandburg, *Bond-orientational Order in Condensed Matter Systems*, Partially ordered systems (Springer-Verlag, 1992) (cit. on p. 35).

[45]D. R. Nelson and B. I. Halperin, «Dislocation-mediated melting in two dimensions», Phys. Rev. B **19**, 2457–2484 (1979) (cit. on p. 35).

[46]A. P. Young, «Melting and the vector coulomb gas in two dimensions», Phys. Rev. B **19**, 1855–1866 (1979) (cit. on p. 35).

[47]J. M. Kosterlitz and D. J. Thouless, «Ordering, metastability and phase transitions in two-dimensional systems», Journal of Physics C: Solid State Physics **6**, 1181–1203 (1973) (cit. on p. 35).

[48]S. Atkinson, F. H. Stillinger, and S. Torquato, «Existence of isostatic, maximally random jammed monodisperse hard-disk packings», Proceedings of the National Academy of Sciences **111**, 18436–18441 (2014) (cit. on p. 36).

[49]A. Ghosh, J. Radhakrishnan, P. M. Chaikin, D. Levine, and S. Ghosh, *Coupled dynamical phase transitions in driven disk packings*, 2022 (cit. on pp. 37, 39, 48, 63).

[50]D. Hexner and D. Levine, «Noise, diffusion, and hyperuniformity», Phys. Rev. Lett. **118**, 020601 (2017) (cit. on p. 38).

[51]M. P. Allen and D. J. Tildesley, *Computer Simulation of Liquids*, edited by O. C. Press (1987) (cit. on p. 39).

[52]A. Nakano, *Linked-List Cell Molecular Dynamics*, `https://aiichironakano.github.io/cs596/01-1LinkedListCell.pdf` (cit. on p. 39).

[53]J. Bezanson, A. Edelman, S. Karpinski, and V. B. Shah, «Julia: a fresh approach to numerical computing», SIAM review **59**, 65–98 (2017) (cit. on p. 39).

[54]R. D. Jacobsen, *VoronoiCells*, `https://github.com/JuliaGeometry/VoronoiCells.jl`, 2017 (cit. on p. 50).